Boundary Layer Measurements of the NACA0015 and Implications for Noise Modeling

Bertagnolio, Franck

Publication date:
2011

Document Version
Publisher's PDF, also known as Version of record

Boundary Layer Measurements of the NACA0015 and Implications for Noise Modeling

Risø-R-Report

Franck Bertagnolio
Risø-R-1761(EN)
January 2011

Risø DTU
National Laboratory for Sustainable Energy

Author: Franck Bertagnolio
Title: Boundary Layer Measurements of the NACA0015 and Implications for Noise Modeling
Division: Wind Energy Division

Risø-R-1761(EN)
January 2011

Abstract (max. 2000 char.):

A NACA0015 airfoil section instrumented with an array of high frequency microphones flush-mounted beneath its surface was measured in the wind tunnel at LM Wind Power in Lunderskov. Various inflow speeds and angles of attack were investigated. In addition, a hot-wire device system was used to measure the velocity profiles and turbulence characteristics in the boundary layer near the trailing edge of the airfoil. The measured boundary layer data are presented in this report and compared with CFD results. A relative good agreement is observed, though a few discrepancies also appear. Comparisons of surface pressure fluctuations spectra are used to analyze and improve trailing edge noise modeling by the so-called TNO model. Finally, a pair of hot-wires were placed on each side of the trailing edge in order to measure the radiated trailing edge noise. However, there is no strong evidence that such noise could be measured in the higher frequency range. Nevertheless, low-frequency noise could be measured and related to the presence of the airfoil but its origin is unclear.

ISSN 0106-2840
ISBN 978–87–550–3656-7

Project/Contract no.:
EUDP-2009- 64009-0272

Group's own reg. no.:
1110076-01

Sponsorship:

Cover :

Pages: 66
Tables: 2
References: 23

Information Service Department
Risø National Laboratory for Sustainable Energy
Technical University of Denmark
P.O.Box 49
DK-4000 Roskilde
Denmark
Telephone +45 46774005
bibl@risoe.dtu.dk
Fax +45 46774013
www.risoe.dtu.dk

Contents

1 Introduction

As part of the EUDP-founded project 'Low Noise Airfoil', this report presents the results obtained during an experimental campaign that was conducted in the wind tunnel at LM Wind Power in Lunderskov from August 16^{th} to 26^{th}, 2010. The goal of this study is to validate the so-called TNO trailing edge noise model through measurements of the boundary layer turbulence characteristics and the far-field noise generated by the acoustic scattering of the turbulent boundary layer vorticies as they convect past the trailing edge.

This campaign was conducted with a NACA0015 airfoil section that was placed in the wind tunnel section. It is equipped with high-frequency microphones beneath its surface so that surface pressure fluctuations generated by the boundary layer turbulence can be measured.

Hot-wire anemometry was used to measure mean flow velocities and turbulent fluctuations inside the boundary layer. For this, a traverse system was developped so that the hot-wire probes could be moved with a step motor perpendicularly to the airfoil chord in order to perform measurements across the boundary layer. The probes could be moved manually back and forth relatively to the inflow velocity and along the trailing edge in order to investigate several locations in the flow field.

As a second part of the experiment, the previous traverse system was removed and two airfoil-shaped probe-holders were installed instead. These were designed to hold in place two hot-wire sensors, one on each side of the trailing edge (below and above the plane spanned by the airfoil trailing edge and the inflow velocity) in an attempt to measure the velocity fluctuations associated to the pressure waves originating from the acoustic scattering at the trailing edge, which should behave as a dipole.

The next section describes the experimental set-up and gives an overview of the measurement data. Turbulent boundary layer measurements are presented in Section 3. These measurements are confronted in Section 4 to CFD calculations as well as to the TNO model that can be used to calculate the airfoil surface pressure fluctuations spectrum. Some of the experimental data measured in the Laminar Wind Tunnel at Stuttgart University are used to complete this study. The previous comparisons are used in order to improve the TNO model predictions. Section 5 gives a short presentation of the attempt to measure trailing edge noise with hot-wire anemometry and the associated results.

2 Experimental Set-up

2.1 LM Wind Power Wind Tunnel

The LM Wind Power wind tunnel is designed for the testing of wind turbine airfoils [19]. The actual test section dimensions are 1.35 m in width, 2.70 m in height, and 7 m in length. A NACA0015 airfoil section with a 0.9 m chord was placed across the width of the tunnel. During this study, three inflow velocities were investigated: $U_\infty = 30$, 40 and 50 m/s, as well as four angles of attack: $\alpha = 0$, 4, 8 and 12^o. Note that the flow temperature was oscillating between approximately 20 and 26^oC during the experiment.

A previous study [19] showed that the inflow turbulence (without turbulence grid in the tunnel as it is the case here) was roughly of the order of $I = 0.1\%$ in all velocity directions at all wind tunnel inflow velocities. A subsequent study [2] using tri-axial hot-wire anemometry showed higher turbulence intensities of approximately 1%.

2.2 Hot-Wire Measurements

Both single-wire and bi-axial hot-wire probes from Dantec Dynamics [11] together with the StreamLine CTA (Constant Temperature Anemometer) measurement system and the StreamWare software were used for data acquisition and post-processing. The traverse system used to explore the boundary layer (BL) with these probes was designed and manufactured at Risø DTU by Andreas Fischer. The whole system with probes installed in the wind tunnel downstream of the airfoil trailing edge (TE) is pictured in Figure 1.

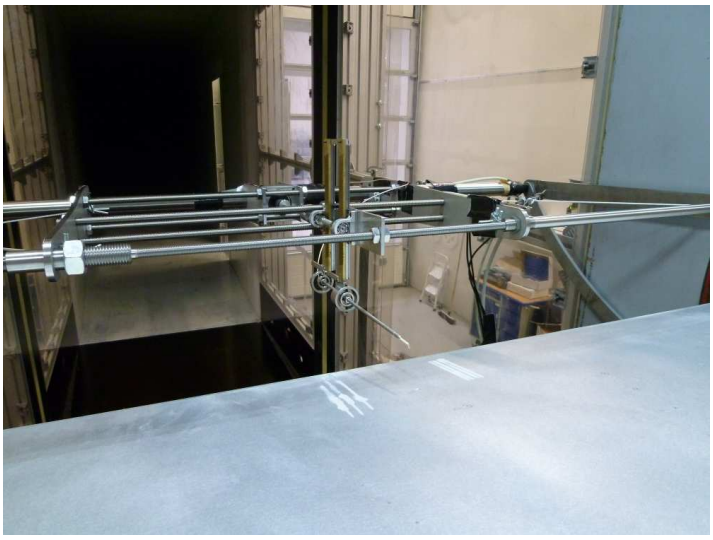

Figure 1. Traverse set-up

As for the far-field sound measurements, two slanted hot-wire probes were fixed at the tip of probe-holders, themselves mounted on the nose of airfoil-shaped holders spanning the whole tunnel width downstream the airfoil TE. The device set-up can be seen in Fig. 2.

Details of the calibration of the hot-wire sensors, as well as temperature corrections and velocity coordinates transformations, are provided in Appendix B. The measurement sampling rate was set to 25 kHz, but a 10 kHz low-pass filter was applied when acquiring the data to avoid aliasing.

Figure 2. Slanted hot-wire holders set-up

In addition, TE noise measurements with hot-wires were performed both in DC and AC mode. In the latter case, various amplification gains were used and a 100 Hz high-pass filter was applied (see Section 5).

2.3 Airfoil Model and Surface Microphones

The NACA0015 airfoil section with a chord $C = 0.9\,\mathrm{m}$ and a spanwise extension $L = 1.35\,\mathrm{m}$ was installed in the wind tunnel. For some cases, a zig-zap (ZZ) tape was placed at 5% chord from the leading edge on the suction side of the airfoil in order to trigger transition.

Sennheiser KE 4-211-2 microphones were flush-mounted beneath the airfoil surface in order to measure the pressure fluctuations. These microphones have a potential sampling frequency larger than 50 kHz. However, the actual sampling rate of the data was set to the same as for the hot-wire probes, i.e. 25 kHz. Note that the low-pass filter couldn't be applied to the microphone measurement data since these were directly acquired through the A/D board and could not be processed by the StreamLine acquisition system. Consequently, the surface pressure measurements may be polluted by some aliasing effects. However, it is believed that this effect is small in our case as the energy contained in the signals at frequencies above 25 kHz is expected to be rather small.

The array of surface microphones consists of 2×38 microphones placed on the each side of the airfoil. During this campaign only 5 microphones were acquired. The locations of the corresponding pressure holes are:

- Microphone M28 : $X/C = 0.833\,,\ z = 615\,\mathrm{mm}$
- Microphone M29 : $X/C = 0.894\,,\ z = 629\,\mathrm{mm}$
- Microphone M30 : $X/C = 0.950\,,\ z = 645\,\mathrm{mm}$
- Microphone M29 : $X/C = 0.978\,,\ z = 655\,\mathrm{mm}$
- Microphone M36 : $X/C = 0.019\,,\ z = 702\,\mathrm{mm}$ (on pressure side)

Note that the number N in their designation 'MN' is related to their number in previous experiments with the same model (see for example [6, 2]). These microphones are all located on the suction side except for the last one located close to the leading edge. Microphones M29 and M30 are connected to the surface holes through a tubing system which requires a special calibration (see Fischer [9]).

2.4 Overview of BL Measurement Data

Three different inflow velocities were considered during the campaign and the respective Reynolds numbers Re based on the airfoil chord are reported in Table 1. The kinematic viscosity is assumed equal to $1.58{\times}10^{-5}\,\mathrm{m}^2/\mathrm{s}$ (air at approximately 23^oC).

U_∞ [m/s]	30.0	40.0	50.0
Re ($\times 10^6$)	1.71	2.28	2.85

Table 1. Inflow velocities and associated Reynolds numbers

The table in Fig. 3 provides an overview of the different measurement cases which are organized in 'series', each of those characterized by specific experimental conditions. The series are denoted as 'ST' (see 1^{st} column in the table), where T is a specific number assigned to each one of them.

For each series, the boundary layer was traversed with the hot-wire probe according to a distance to the wall distribution which name is specified in the last column. The actual positions can be found in Appendix A. The number in parentheses refers to the number of measurement points across the BL. Note that the number of points for the 'Original' series S01 and S02 is larger than for S03 as the two first series include points both on the suction and pressure side of the airfoil, whereas the third one only includes points on the suction side.

The 5^{th} column 'Yref' gives the distance from the airfoil wall surface to the first measurement point. It is an offset that has to be added to the positions given in Appendix A.

The 6^{th} column 'Y-axis' refers to the X-wires probe (denoted as 'XN' in the 2^{nd} column) being orientated vertically or horizontally. In the former case it measures both u_x and u_y, in the latter u_x and u_z. For series S15, BL denotes the fact that a boundary layer probe type is used. Its single hot-wire is parallel to the airfoil surface and perpendicular to the incoming mean flow.

The 4^{th}column 'X/C' specifies the position of the probe chordwise, whereas the 7^{th} column specifies its position in the width of the wind tunnel. The microphone designation in parentheses refers to the one which is directly upstream of the hot-wire probe.

Series	Probe type	Airfoil	X/C	Yref [mm]	Y-axis	Z [mm]	BL distrib.
S01	XN	Clean	1.044	0	Vertical	655(M31)	Original(24)
S02	XN	Clean	1.044	0	Vertical	629(M29)	Original(24)
S03	XN	Clean	1.044	0	Horizontal	629(M29)	Original(16)
S04	XN	Clean	0.91	3	Vertical	629(M29)	Extended(16)
S05	XN	Clean	0.91	3	Horizontal	629(M29)	Extended(16)
S06	XN	ZZ-tape	0.91	3	Horizontal	629(M29)	Extended(16)
S07	XN	ZZ-tape	0.91	3	Vertical	629(M29)	Extended(16)
S08	XN	ZZ-tape	0.91	3	Vertical	629(M29)	DBL(10)
S09	XN	ZZ-tape	0.97	3	Vertical	629(M29)	DBL(10)
S10	XN	ZZ-tape	0.995	3	Vertical	629(M29)	DBL(10)
S11	XN	ZZ-tape	1.003	3	Vertical	629(M29)	DBL(10)
S12	XN	Clean	1.003	3	Vertical	629(M29)	DBL(10)
S13	XN	Clean	0.995	3	Vertical	629(M29)	DBL(10)
S14	XN	Clean	0.91	3	Vertical	629(M29)	DBL(10)
S15	BL	Clean	0.91	1.5	Vertical	629(M29)	DBL(10)

Figure 3. Series experimental conditions details

The table in Fig. 4 provides the inflow velocities and angles of attack that were actually measured for each individual series.

Series S01	00 [degs]	04 [degs]	08 [degs]	12 [degs]
30 [m/s]	x	x	x	x
40 [m/s]	x	x	x	x
50 [m/s]	x	x	x	x

Series S02	00 [degs]	04 [degs]	08 [degs]	12 [degs]
30 [m/s]	x		x	
40 [m/s]		x	x	
50 [m/s]	x		x	x

Series S03	00 [degs]	04 [degs]	08 [degs]	12 [degs]
30 [m/s]				x
40 [m/s]		x	x	
50 [m/s]	x			x

Series S04	00 [degs]	04 [degs]	08 [degs]	12 [degs]
30 [m/s]	x		x	x
40 [m/s]		x	x	x
50 [m/s]	x		x	x

Series S05	00 [degs]	04 [degs]	08 [degs]	12 [degs]
30 [m/s]	x			x
40 [m/s]		x	x	
50 [m/s]	x			x

Series S06	00 [degs]	04 [degs]	08 [degs]	12 [degs]
30 [m/s]				
40 [m/s]		x	x	
50 [m/s]	x			x

Series S07	00 [degs]	04 [degs]	08 [degs]	12 [degs]
30 [m/s]	x		x	x
40 [m/s]		x	x	x
50 [m/s]	x		x	x

Series S08	00 [degs]	04 [degs]	08 [degs]	12 [degs]
30 [m/s]			x	
40 [m/s]	x	x	x	x
50 [m/s]			x	

Series S09	00 [degs]	04 [degs]	08 [degs]	12 [degs]
30 [m/s]			x	
40 [m/s]	x	x	x	x
50 [m/s]			x	

Series S10	00 [degs]	04 [degs]	08 [degs]	12 [degs]
30 [m/s]			x	
40 [m/s]	x	x	x	x
50 [m/s]			x	

Series S11	00 [degs]	04 [degs]	08 [degs]	12 [degs]
30 [m/s]			x	
40 [m/s]	x	x	x	x
50 [m/s]			x	

Series S12	00 [degs]	04 [degs]	08 [degs]	12 [degs]
30 [m/s]			x	
40 [m/s]	x	x	x	x
50 [m/s]			x	

Series S13	00 [degs]	04 [degs]	08 [degs]	12 [degs]
30 [m/s]			x	
40 [m/s]	x	x	x	x
50 [m/s]			x	

Series S14	00 [degs]	04 [degs]	08 [degs]	12 [degs]
30 [m/s]			x	
40 [m/s]	x	x	x	x
50 [m/s]			x	

Series S15	00 [degs]	04 [degs]	08 [degs]	12 [degs]
30 [m/s]	x		x	
40 [m/s]	x	x	x	x
50 [m/s]	x		x	

Figure 4. Measured velocities and angles of attack for each series

2.5 Data Post-Processing

The calibration of the hot-wires and calculation of the velocity time-series from the hot-wire voltage outputs are described in Appendix B.

A brief summary of the theory that is used to analyze the BL flow turbulence is reported in Appendix C. The theoretical developments are mostly based on the spectral theory of turbulence. The assumptions of homogeneity and isotropy are often required to obtain analytical solutions.

In the following of this report, some figures display various quantities as a function of the distance to the wall/airfoil surface. It should be noted here that the actual value that is used in the figures is the distance of the hot-wire probe to the reference point, the latter being located on the wall itself ($y = 0$), but for an obvious reason it is never visited by the probe. Note that even if the probe is moving perpendicularly to the airfoil chord, the data have been projected onto the normal to the wall (see Appendix A for details).

The previous change of coordinates is also taken into account for the velocity components that are displayed in the figures of this report. As a result, the subscripts x, y, and z of the velocity components refer to the direction parallel to the airfoil surface and aligned with the main flow direction, the direction perpendicular to the airfoil surface, and the direction along the trailing edge, respectively. The variable X will refer to the actual chord axis.

3 Turbulent Boundary Layer Measurements

This chapter concentrates on the display and analysis of the velocity measurements with the X-wires probe in the turbulent boundary layer over the NACA0015 airfoil section as well as the surface pressure measurements.

Two distinct experimental conditions are studied. In one case, the airfoil surface is clean. In the second one, a zig-zag (denoted ZZ hereafter) tape was placed at 5% of the airfoil chord (on the suction side only) in order to trigger transition to turbulence.

3.1 Influence of the ZZ-Tape

Figure 5 show the mean velocity profiles U_x across the BL measured at $U_\infty = 40$ m/s for the various angles of attack. Each subfigure displays these profiles at three different locations along the airfoil chord: $X/C = 0.91$, 0.995 and 1.003. It can be observed that the introduction of the ZZ-tape is slowing down the boundary layer velocity quite noticeably, though for some unknown reason this is less pronounced at $\alpha = 8^o$. It can also be seen that the velocity profiles remain almost unchanged between the locations $X/C = 0.995$ and 1.003.

In the same cases as above, Figs. 6(a) and (b) respectively show the turbulent stresses $< u_x u_x >$ and $< u_y u_y >$. It can be observed that the ZZ-tape significantly increases the turbulence intensities as it could be expected. Again, it seems that the case $\alpha = 8$ is less subject to this influence.

Figs. 7(a) and (b) respectively show the integral length scales L_x and L_y (see their definitions in Appendix C) for the same cases as above. It can be seen that the ZZ-tape has a general tendency to increase these length scales, though it is not always the rule depending on the position across the BL. It should be noted that in some cases, the integral length scale is diverging to high values at the edge of the BL and above (for L_x at $\alpha = 12^o$ and for L_y at all angles of attack). This is believed to be non-physical as the turbulence should become insignificant outside the boundary layer, and it is probably originating from numerical errors or divergence of the integrals when evaluating these length scales.

As a general conclusion concerning the previous data, it should be noted that in all cases the BL characteristics evolve significantly from the chord position $X/C = 0.91$ as one is getting nearer to the trailing edge ($X/C = 0.995$, 1.003). The BL slightly thickens and the mean velocity decreases. At the same time, the turbulence intensity increases and its peak value location moves away from the airfoil surface. This should be taken into account, for example if using experimental data from the upstream position for trailing edge noise modeling which is related to BL characteristics in the vicinity of the trailing edge.

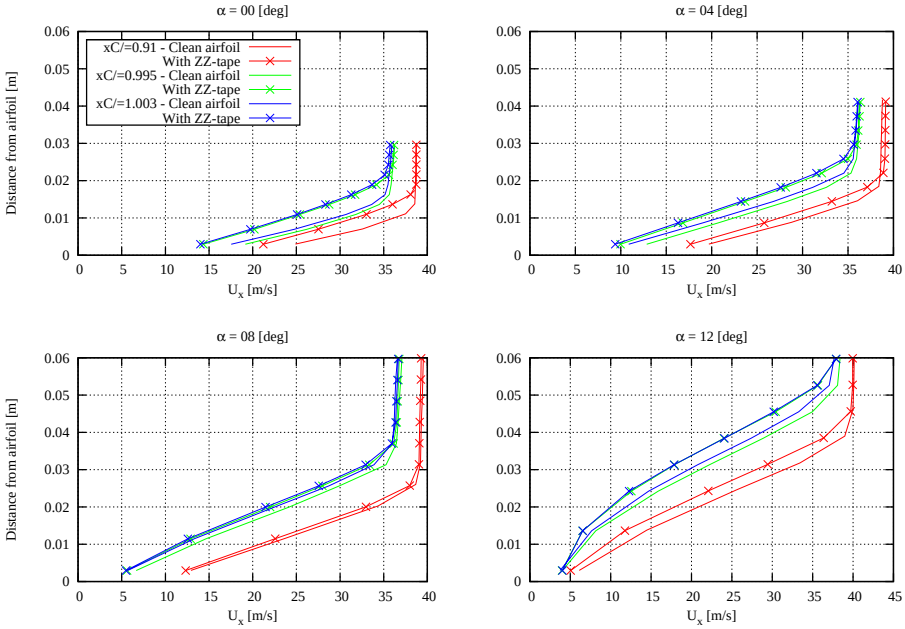

Figure 5. Influence of ZZ-tape on velocity profile U_x at $U_\infty = 40\ m/s$

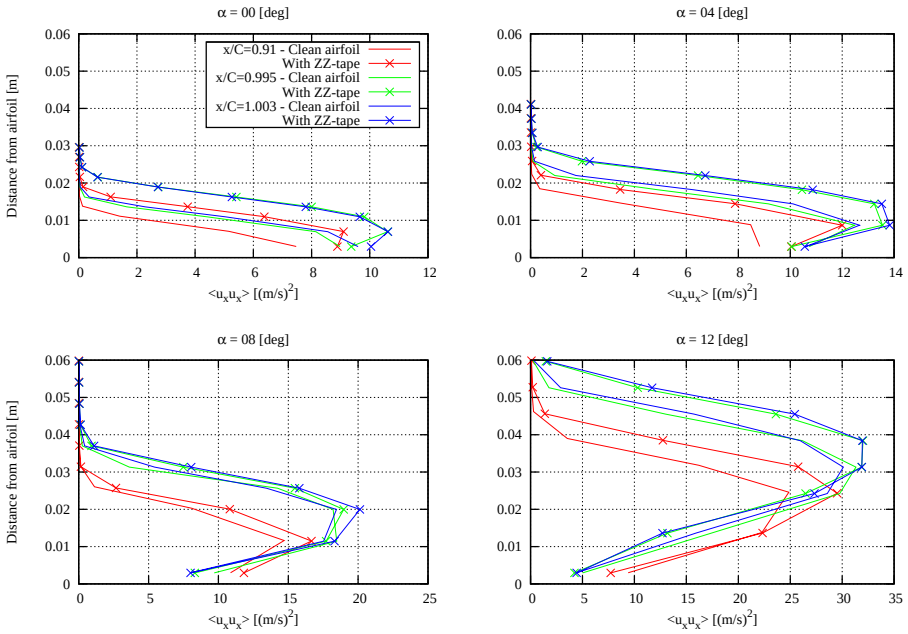

(a) Turbulent stress $< u_x u_x >$

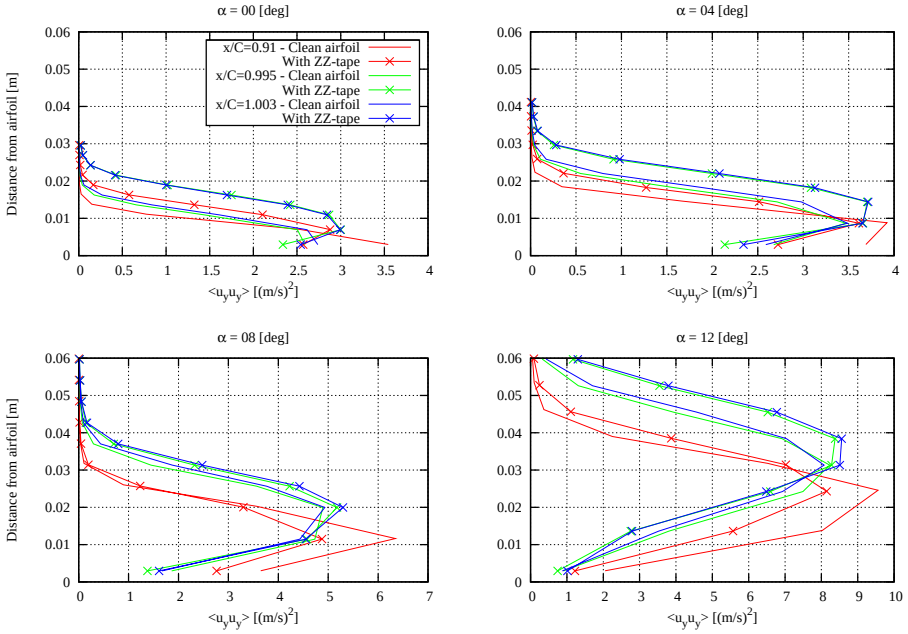

(b) Turbulent stress $< u_y u_y >$

Figure 6. Influence of ZZ-tape on turbulent stresses at $U_\infty = 40\ m/s$

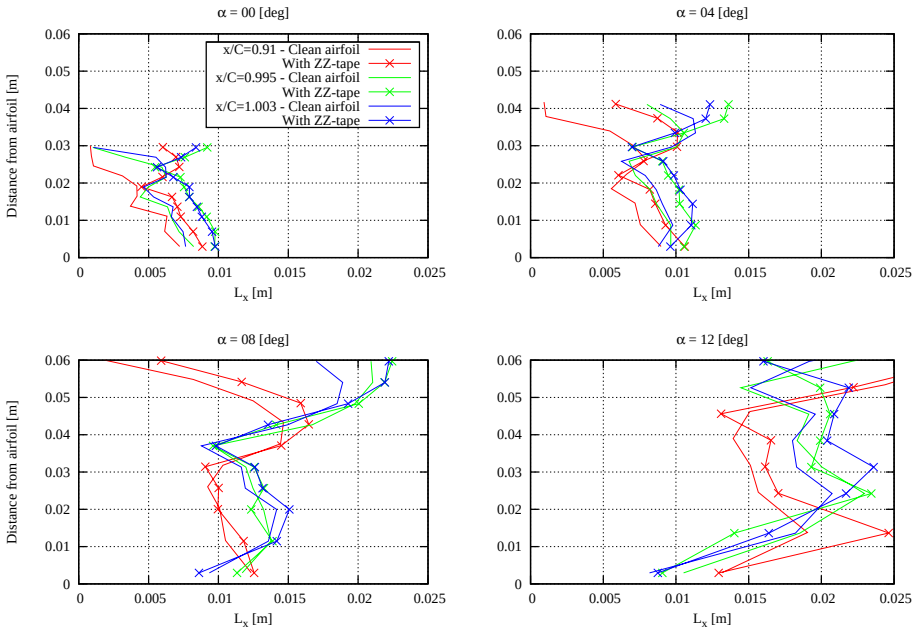

(a) Integral length scale L_x

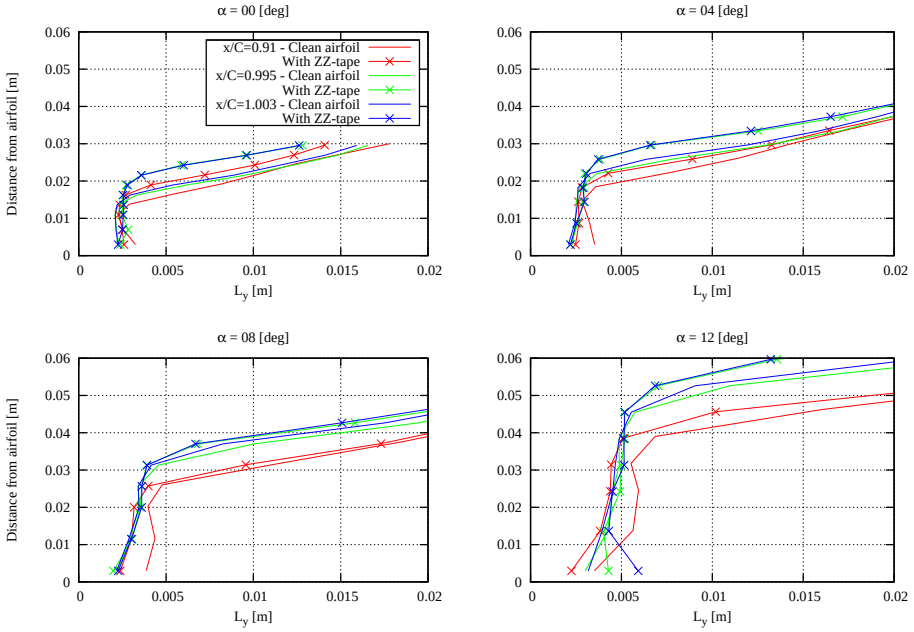

(b) Integral length scale L_y

Figure 7. Influence of ZZ-tape on integral length scales at $U_\infty = 40\ m/s$

3.2 One-Point Velocity Spectra

One-point velocity power spectra for the three velocity components u_x, u_y and u_z are compared in Fig. 8(a) for the two first components, and in Fig.8(b) for the first and the third. Note that these spectra are only displayed for three different measurement points across the BL, involving the point closest to the surface, a second one a bit further away close to where the turbulent kinetic energy peaks, and a third one even further away from the surface where the turbulent kinetic energy is not quite so strong. It turns out that the position closest to the surface where the probes could be positioned is already quite far away from the surface. As a consequence, the first measurement point is already close to where the turbulent kinetic energy peaks for the two first angles of attack $\alpha = 0$ and 4^o. At higher angles of attack, the boundary layer is getting thicker and it is possible to observe more accurately the turbulent energy peak. In addition, note that the inflow velocity is equal to 50 m/s for the angles of attack $\alpha = 0$ and 12^o, and 40 m/s for $\alpha = 4$ and 8^o. All data were measured at the chord location $X/C = 0.91$.

It can be observed that the isotropic assumption is only valid at higher frequencies (> 2000 to 3000 Hz). This may indicate the existence of an isotropic inertial sub-range at higher frequencies (i.e. at higher wavenumbers). At lower frequencies, the first component u_x is always more energetic than the two others.

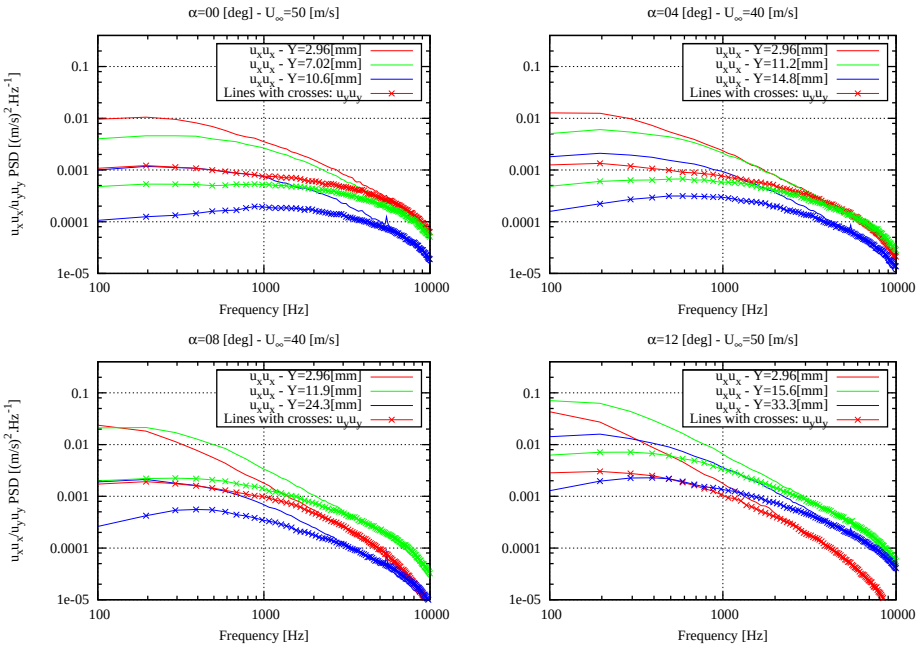

(a) u_x and u_y components

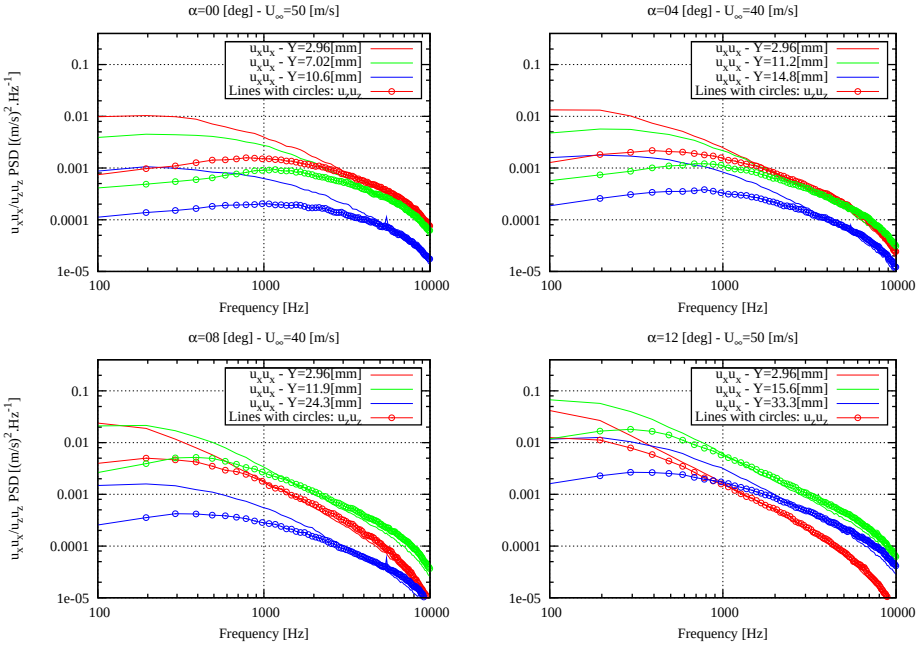

(b) u_x and u_z components

Figure 8. One-point velocity spectra

3.3 Cross-Spectral Characteristics between Velocity Components

For the same cases as in the previous section, the cross-spectra, coherence and phase between the u_x and the u_y components are displayed in Figs. 9, 10(a) and 10(b), respectively. Those for the u_x and u_z components are displayed in the same figures, but using lines with circles (only circles for the phase plots).

It can be seen that the velocity components are correlated at all frequencies, though the coherence is in general higher at lower frequencies. The u_x and u_y components are always more correlated than the u_x and u_z components. Interestingly, the phase shift between the various components is changing noticeably as a function of the distance to the wall. This confirms the obvious fact that the flow is inhomogeneous in that direction, but also indicates that the turbulence characteristics, in particular with respect to isotropy, are changing across the BL.

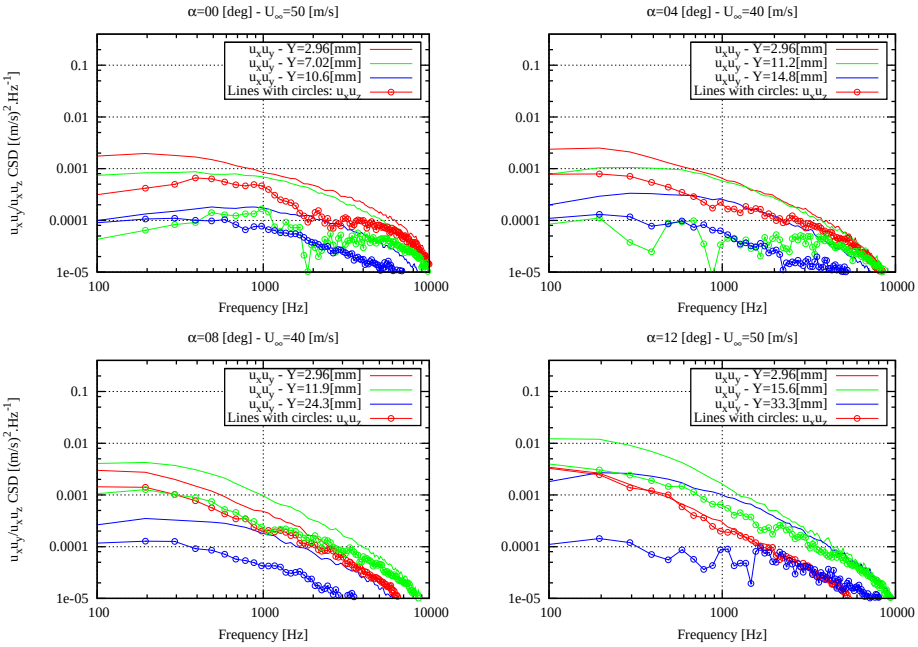

Figure 9. Cross-spectra for $u_x - u_y$ and $u_x - u_z$ components

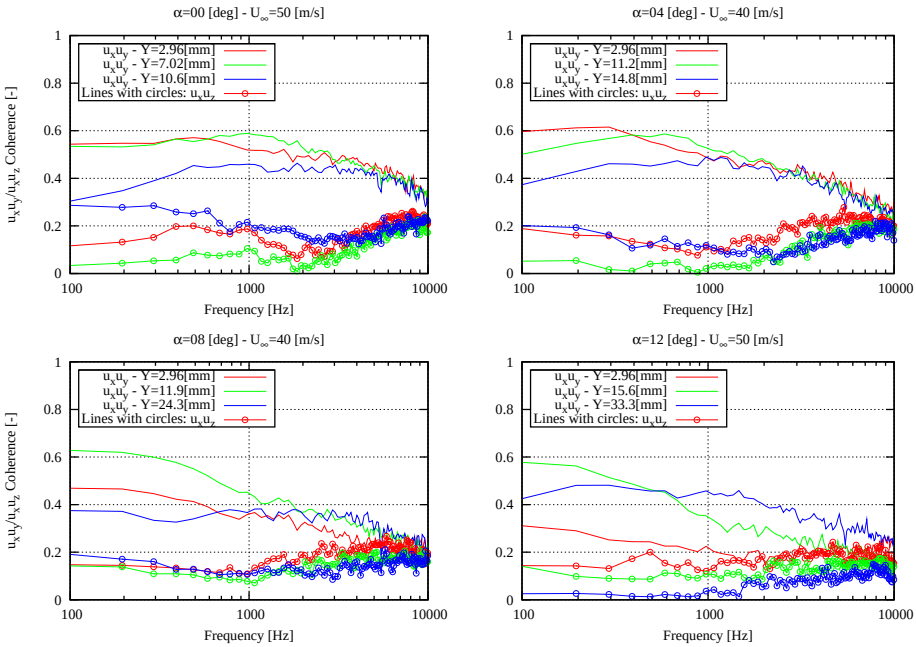

(a) Coherence

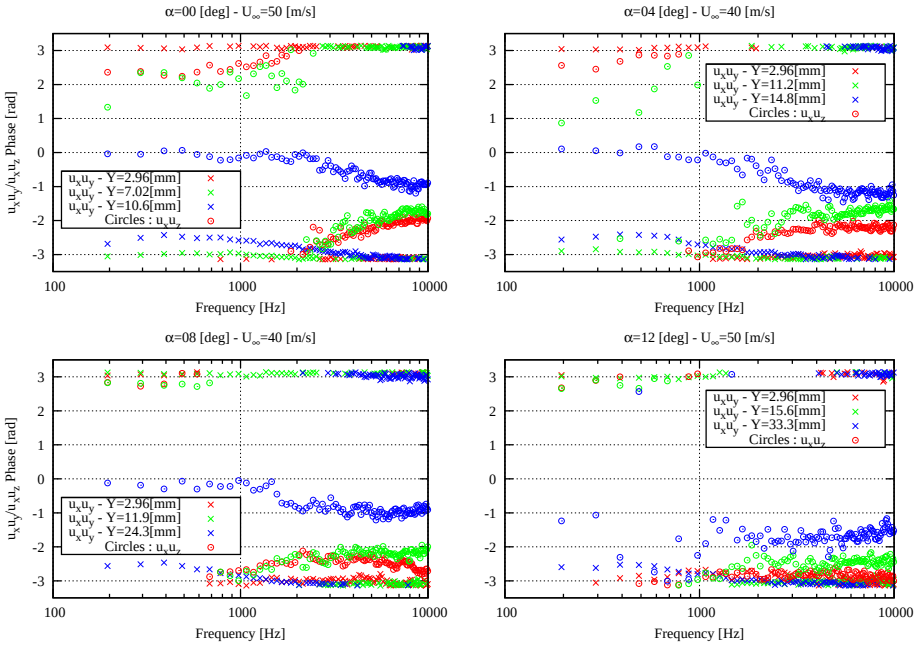

(b) Phase

Figure 10. Coherence/Phase between $u_x - u_y$ and $u_x - u_z$ components

3.4 Coherence/Phase between Surface Pressure and Velocity

The cross-correlations between the measured surface pressure from microphone M30 located at $X/C = 0.894$ and the velocity components measured with the hot-wire probe at $X/C = 0.91$ are calculated. Note that the displayed data originates from series S04/S05 for which the microphone M30 is directly upstream the hot-wire probe location. The velocity locations across the BL are the same as in the two previous sections.

Figs. 11(a) and (b) show the coherence and phase between the surface pressure and the horizontal component u_x, respectively. Figs. 12(a) and (b) show the same functions for the vertical component u_y.

It can be seen that there exists a relatively good correlation between the surface pressure and the velocity up to at least 2000 Hz, higher in some cases in particular for the u_y component. Note that the coherence calculated for the u_y component is always higher than for the u_x component. This is in accordance with the fact the surface pressure fluctuations are determined by the latter component according to the theory for the flat plate (see Appendix D).

Surprisingly, below 1000 Hz and mostly for the u_y component, the coherence increases as the velocity component is measured further away from the airfoil surface. This is probably due to the fact that the turbulent energy contained in the velocity component is decreasing as one goes away from the airfoil surface, while the wall pressure fluctuating energy remains obviously constant.

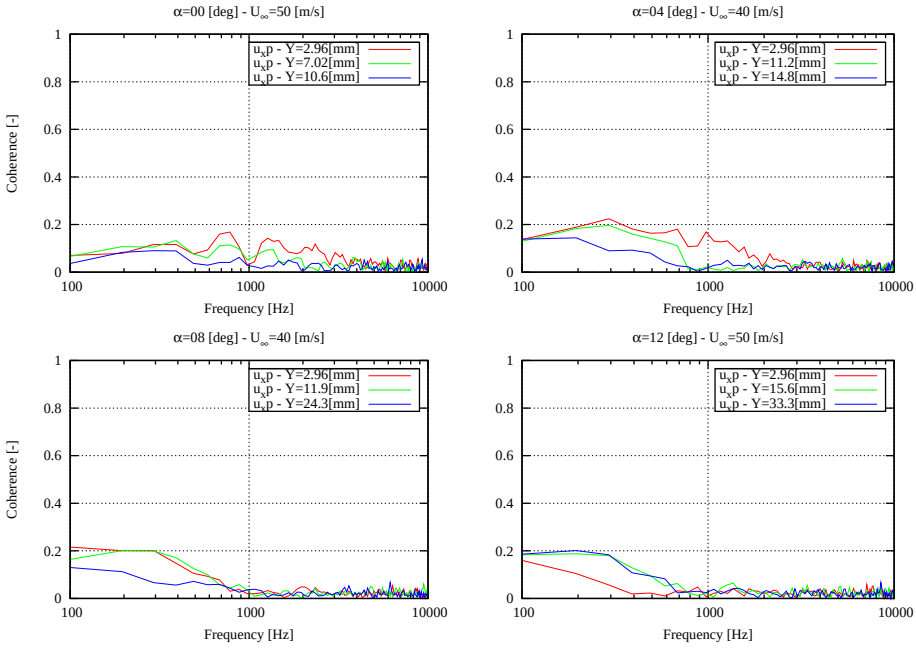

(a) Coherence

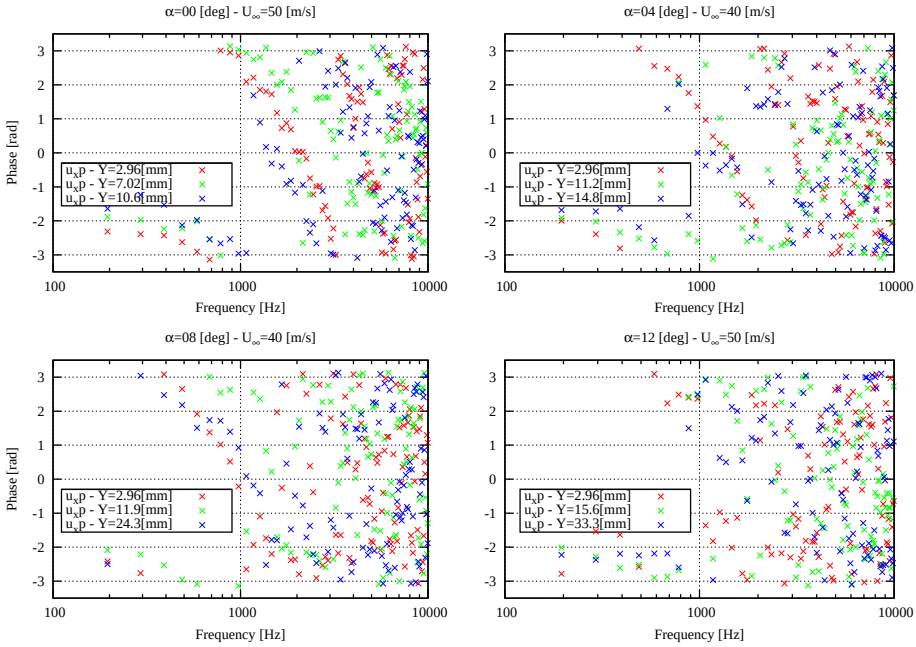

(b) Phase

Figure 11. Coherence/Phase between surface pressure-u_x component

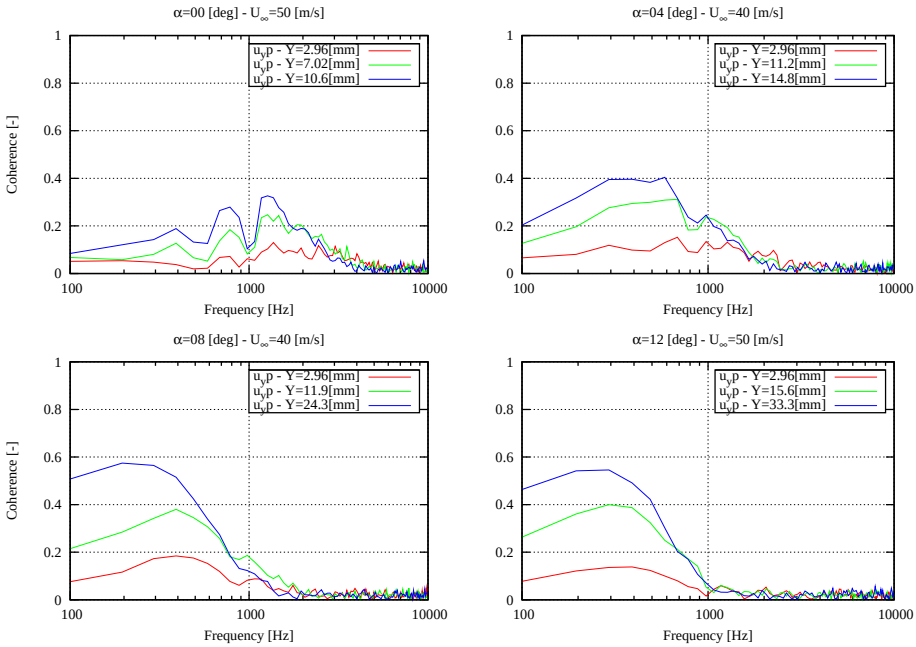

(a) Coherence

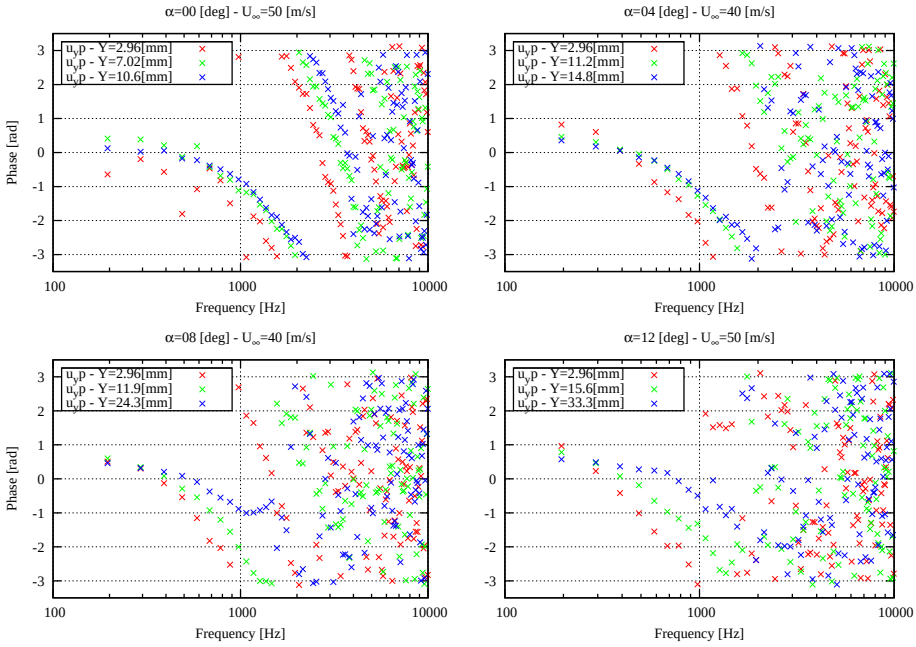

(b) Phase

Figure 12. Coherence/Phase between surface pressure-u_y component

4 Measurement vs. Model Comparisons

This section concentrates on comparison between the measured data (i.e. BL velocity components and surface pressure) and numerical modeling.

In a first step, CFD calculations are performed with the two-dimensional Reynolds Averaged Navier-Stokes solver EllipSys2D [22, 17, 18] using the $k-\omega$ SST turbulence model [16]. For comparison with the clean airfoil, the e^n transition model by Drela and Giles [8] is used. In the case of a ZZ-tape placed on the airfoil suction side, transition is fixed at the same location than the tape, i.e. at 5% chord. Mean velocity profiles and averaged turbulent quantitities are compared with measurements. In addition, the velocity spectra measured in the wind tunnel are compared with the isotropic theoretical spectra of Von Karman (or other similar derivation) for which the turbulent kinetic energy (or turbulent stresses) and length scales are extracted from the CFD calculations or the measurement data.

In a second step, the results from the previous CFD calculations can be used as input for the TNO model that provides an estimation of the surface pressure spectra (in addition to the far field noise spectra).

4.1 Comparison with CFD Calculations

CFD results are compared with the clean airfoil experimental results. Note that the results displayed for $\alpha = 0$ and 12^o were obtained with the inflow velocity $U_\infty = 50\,\mathrm{m/s}$, and those for $\alpha = 4$ and 8^o with $U_\infty = 40\,\mathrm{m/s}$.

The mean velocity and turbulent kinetic energy (TKE) profiles are plotted in Figs. 13 and 14, respectively. The TKE for the experimental results is obtained by adding the turbulent stresses in all directions and dividing by 2. Although the computational and experimental mean velocity profiles are quite similar, the velocity difference at one given BL position can be quite large. This may be caused by a wrong offset specification of the initial probe position when exploring the BL (see Section 2.4). As for the TKE, it can be observed that the differences between computational and experimental results increase with increasing angle of attack.

The turbulent stresses in the three space directions are displayed in Figs. 15(a-b-c). Isotropy is assumed for the CFD results, that is:

$$< u_i u_i > = \frac{2}{3} k_T \qquad \text{for} \quad i = x, y, z$$

It is clear that the flow is highly anisotropic. The u_x component is noticeably more energetic than the two others, whereas the u_z component is slightly more energetic than the u_y component.

A wind tunnel blockage effect could have explained some discrepancies. However, it appears that the differences in maximum mean velocity at the top of the BL between the measurements and the calculations (see Fig. 13) are rather small. Nevertheless, the measured maximum velocity slowly overtakes the computed one as the angle of attack increases. This could be expected since the blockage effect is intensified when the apparent surface of the airfoil relatively to the incoming flow, which is directly related to the angle of attack, increases.

The integral length scales L_x, L_y and L_z are displayed in Fig. 16(a-b-c), respectively. As for the CFD estimation, the same value is plotted for the three length scales using Eq. (D.22) (see Appendix D.3). It should be noted here that L_2 is formally defined in Appendix D as the integral length scale of the u_y in the y-direction (but is calculated assuming isotropy), whereas the experimental value L_y has been evaluated using u_y auto-correlation along the local mean flow

direction x using the frozen turbulence hypothesis (see Appendix C). Therefore, a perfect agreement between the measured and computed integral length scales (more precisely between L_y and L_2) should not be expected.

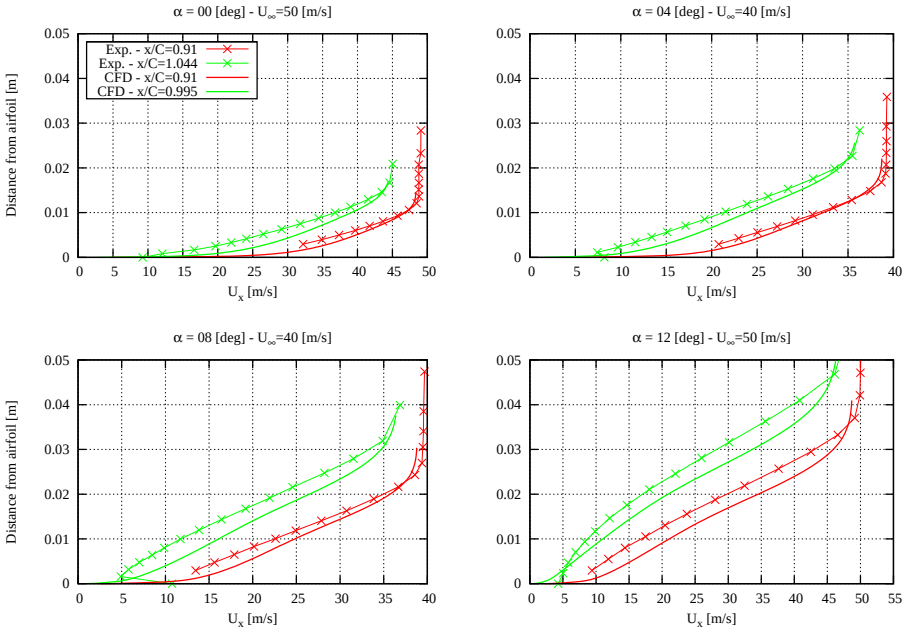

Figure 13. Velocity profile U_x

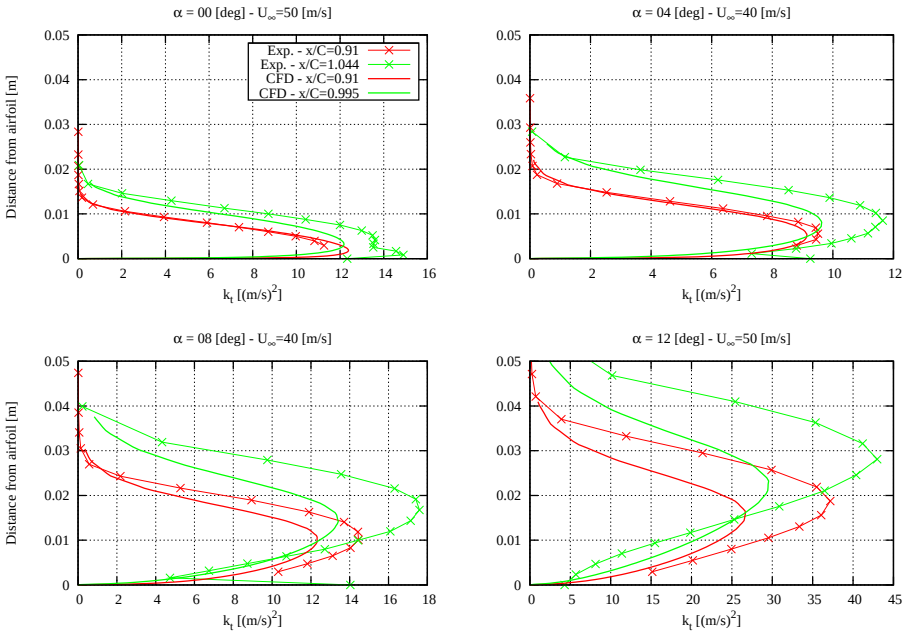

Figure 14. Turbulent kinetic energy k_T

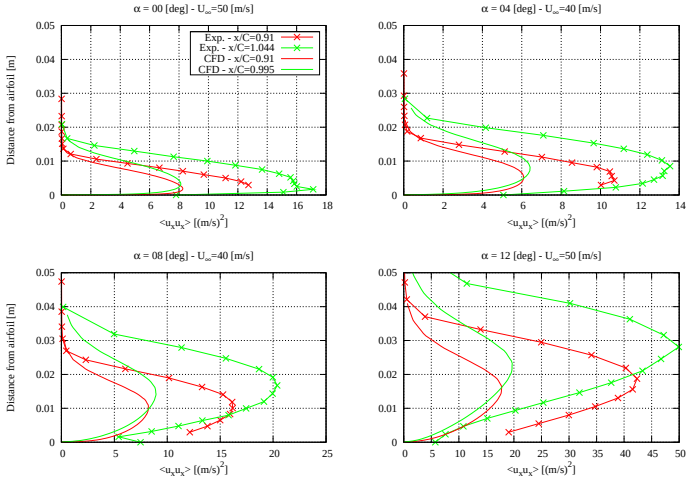

(a) Turbulent stress $< u_x u_x >$

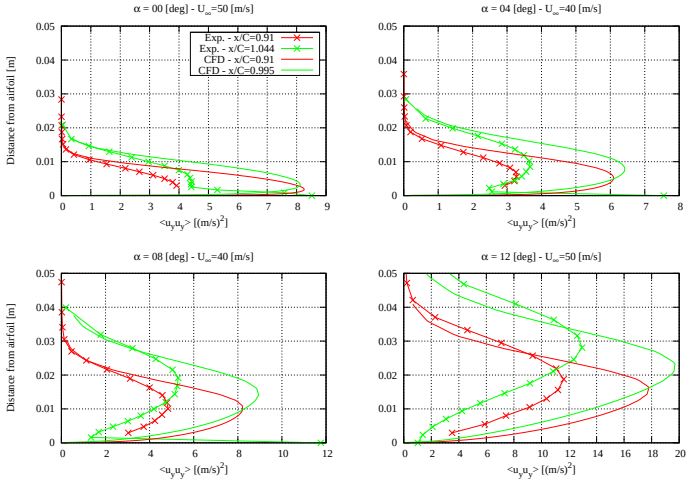

(b) Turbulent stress $< u_y u_y >$

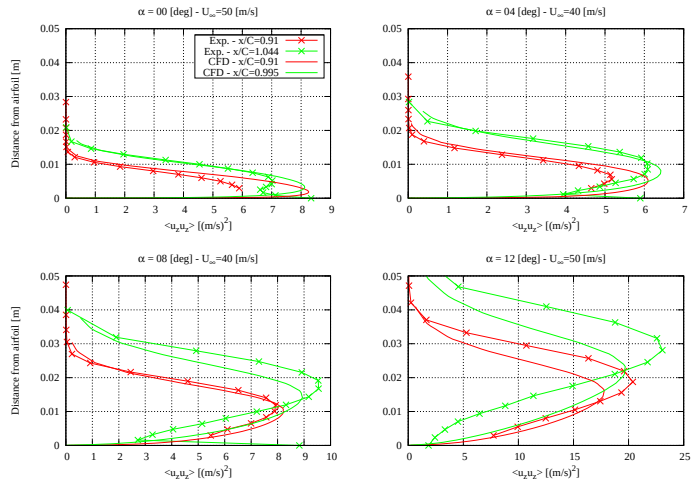

(c) Turbulent stress $< u_z u_z >$

Figure 15. Turbulent stresses (CFD: $< u_i u_i >= 2/3 \cdot k_T$)

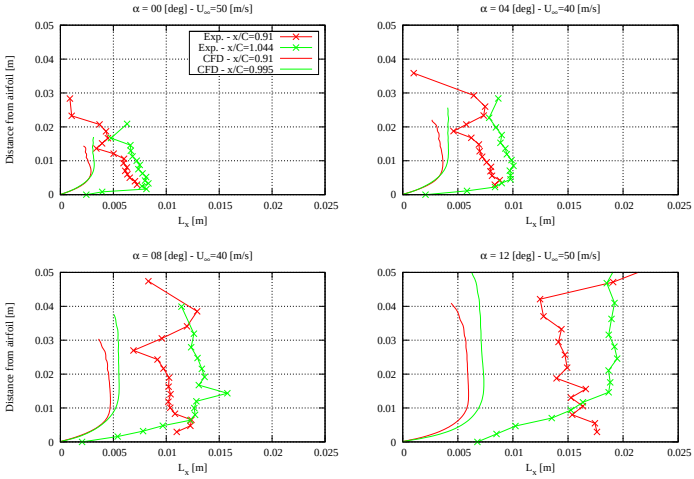

(a) Integral length scales L_x and L_2

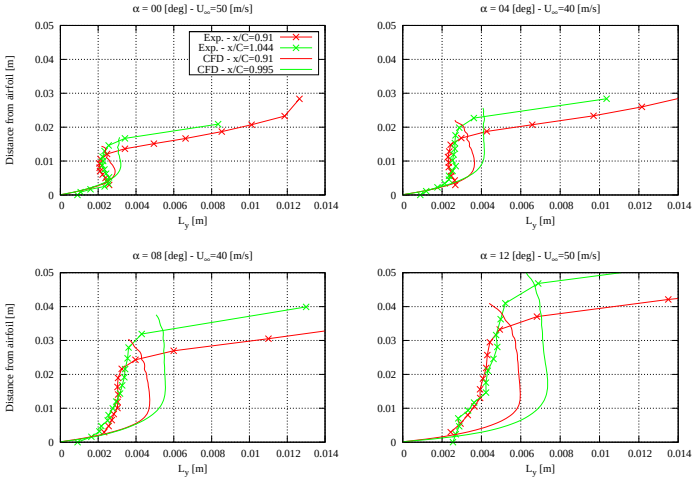

(b) Integral length scales L_y and L_2

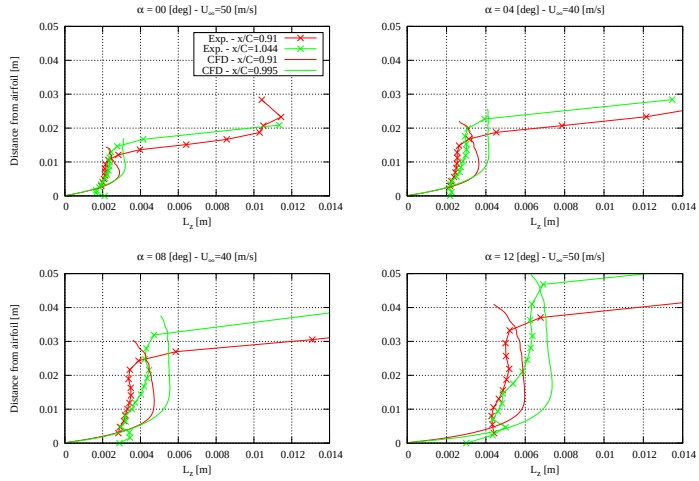

(c) Integral length scales L_z and L_2

Figure 16. Integral length scales $L_{x,y,z}$ (Exp.) and L_2 (CFD)

4.2 Influence of Transition Model on CFD Calculations

In the previous section, it was observed that the TKE predicted by CFD calculations was largely underestimating the experimental values, in particular as the angle of attack increases. A possible explanation for these discrepancies might be a wrong prediction of the transition location in the CFD calculation. Using the e^n transition model by Drela and Giles [8], it is possible to model the turbulence level in the incoming flow by adjusting the so-called N_{crit} factor and thereby modify the transition location. In the previous section, the standard value $N_{\text{crit}} = 9$, corresponding to a very low turbulence level ($I = 0.07\%$), was used. In addition, the value $N_{\text{crit}} = 3$ is used here, which corresponds to a quite large inflow turbulence of $I = 0.85\%$ (at least larger or equal to the actual background turbulence in the LM wind tunnel).

The mean velocity and TKE profiles are plotted in Figs. 17 and 18, respectively, at the chordwise location $X/C = 0.91$. The experimental data are shown for the clean airfoil.

Looking at the velocity profiles, it can be seen that at low angle of attack, the CFD calculations with $N_{\text{crit}} = 9$ are in better agreement with the measurements, but as the angle increases (in particular at $\alpha = 12^o$), the case with $N_{\text{crit}} = 3$ show a better agreement. The same conclusion can be drawn for the TKE profiles at the lower angle of attack $\alpha = 0$ and 4^o. However, for the larger angles of attack, the increase in turbulence intensity (or reduction of the N_{crit} factor) can not explain the measured higher TKE values.

Two possible explanations for the previous results emerge: either the CFD turbulence and/or transition models do not reproduce correctly the measured values of the TKE (in particular at higher angle of attack), or the measurement technique is in some way corrupted and overpredict the actual TKE (but this error should be consistent and not depend of the angle of attack...). In addition, a combination of the two previous cases is also an option.

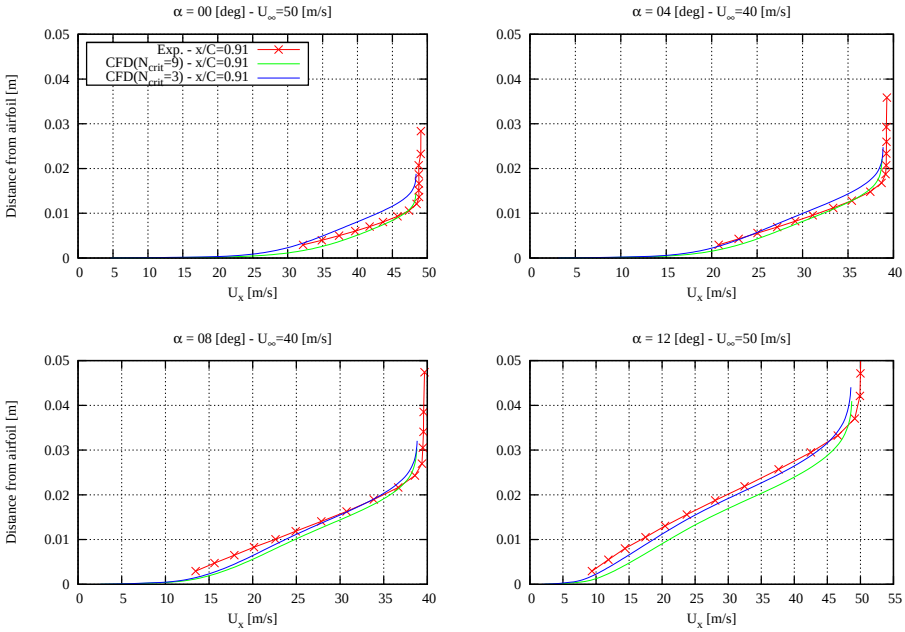

Figure 17. Velocity profile U_x

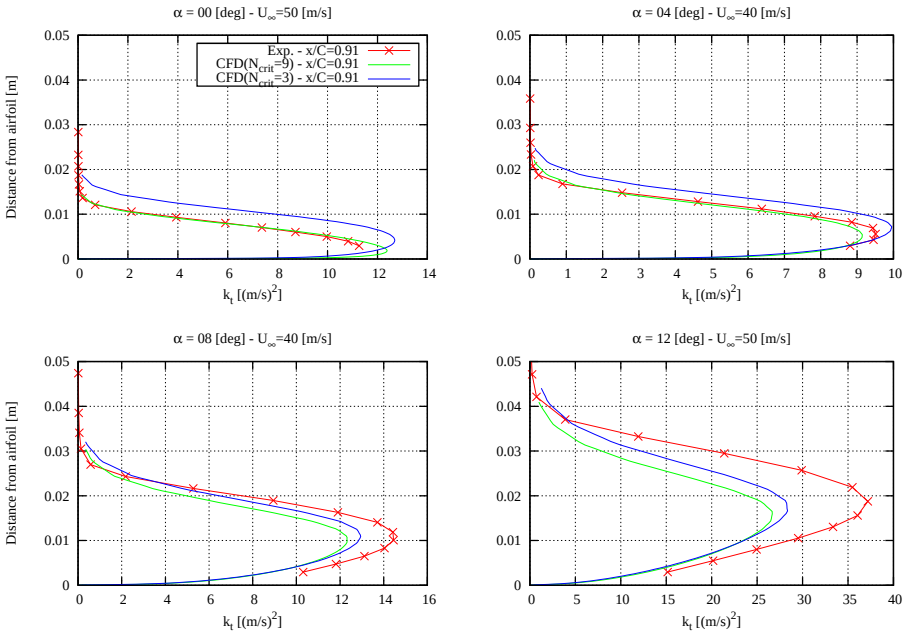

Figure 18. Turbulent kinetic energy k_T

4.3 Measured Velocity and Isotropic One-Point Spectra

For the same cases as in the previous section, the 'pre-multiplied' (see definition below) one-point spectra of the u_x and u_y components are compared with those predicted by the theory of Von Karman for which isotropy is assumed. Note that the spectra displayed in this section are plotted as functions of the wavenumber k_1 which is parallel to the mean flow direction. By assuming frozen turbulence, the following relationship is used:

$$k_1 = 2\pi f / U_x$$

where f is the frequency and U_x is the local mean flow velocity. In addition, all spectra are 'pre-multiplied' by k_1 in order to make their peak wavenumber value, which is characteristics of the integral length scale (see Appendix C), appear more clearly in the figures.

The definition of the Von Karman spectrum requires the variance of the considered velocity component, as well as the corresponding integral length scale. These can be extracted either from the experimental or from the CFD calculation results. These data (turbulent stress and integral length scale) are displayed in Section 4.1 for the clean airfoil. As mentioned above, the peak value wavenumber of the spectra is characteristic of the integral length scale, whereas the amplitude of the spectra is characteristic of the turbulence intensity (variance) of the specific velocity component.

Fig. 19(a) shows the spectra for the u_x component, and Fig. 19(b) for the u_y component. The Von Karman spectra are evaluated using the experimental turbulent stresses and integral length scales. The agreement between the experimental and theoretical spectra is very good for the u_x component. As for the u_y component, the figures indicate in most cases a shift of the theoretical spectra toward higher wavenumbers, indicating that the evaluated integral length scale is too small or alternatively, that the Von Karman spectrum is not a good approximation for this component.

Fig. 20(a-b) show the same spectra as above for the u_x and u_y components, respectively. However, the Von Karman spectra are now evaluated using the turbulent stresses and integral length scales extracted from the CFD calculations. It must be noted here that these data were not extracted at the same distance to the wall for which the measured spectra are shown, but where the mean flow velocities coincide (The actual BL locations are indicated in the figure's legends). This is done because some small errors in the offset defining the initial distance of the probe to the wall yield large error in the turbulent quantities evaluation, since these quantities vary very rapidly close to the wall. In addition, the CFD calculations only give access to the vertical integral length scale L_2 (see section D) and the turbulent kinetic energy. Here, isotropy is assumed and the same values are used in both x and y-directions . The following computational values are used as input for the Von Karman one-point spectra definition of Appendix C:

$$L = \frac{1}{0.7468} L_2 \qquad \text{and} \qquad \sigma_{1c}^2 = < u_i u_i > = \frac{2}{3} k_T$$

The agreement is now much more mitigated than before. As for the u_x component, there exists a noticeable shift of the theoretical spectra toward higher wavenumbers and the amplitudes of the theoretical spectra seem also to be largely underestimated. As for the u_y component, the agreement is slightly better, but a small shift of the theoretical spectra to the higher wavenumber still exists and this time, their amplitudes is slightly overestimated. These remarks apply to the two locations closest to the surface. Conclusions are somehow different for the location furthest away (but this is less critical, as far as the TNO model is concerned, since

the influence of this location on the surface pressure is largely reduced due to its larger distance to the wall and the local turbulence intensity is relatively low anyway).

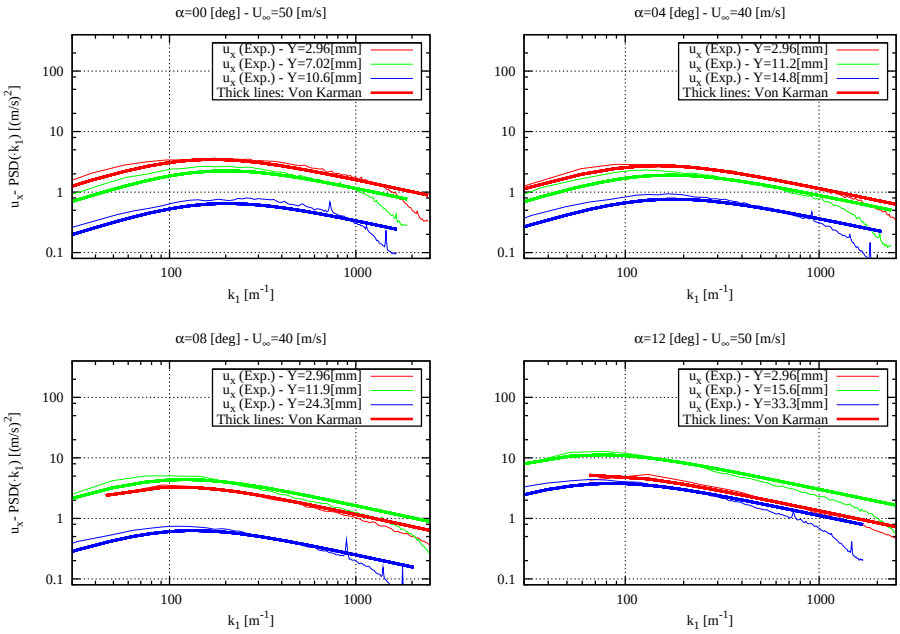

(a) u_x component

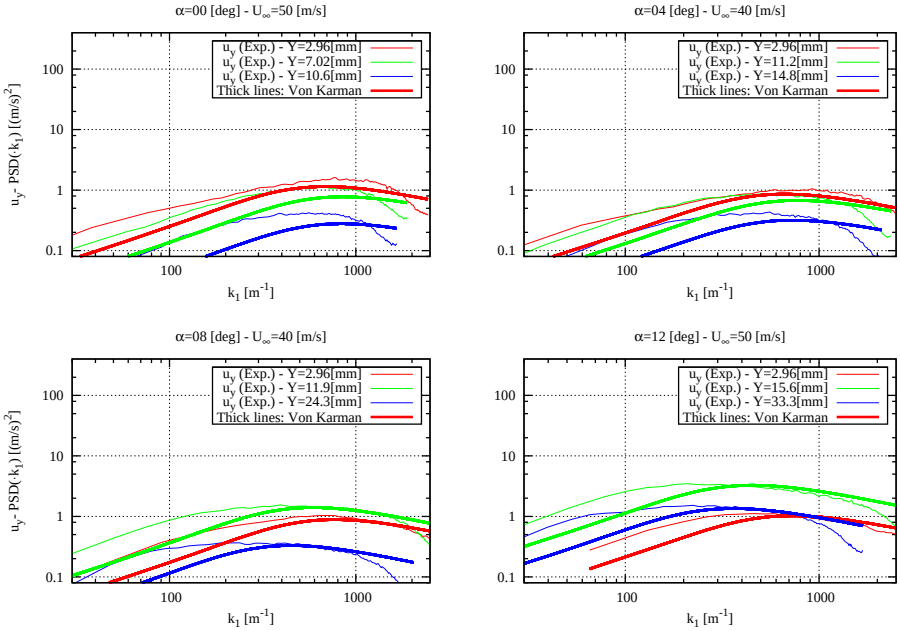

(b) u_y component

Figure 19. Pre-multiplied one-point spectra (V.K. using experimental data)

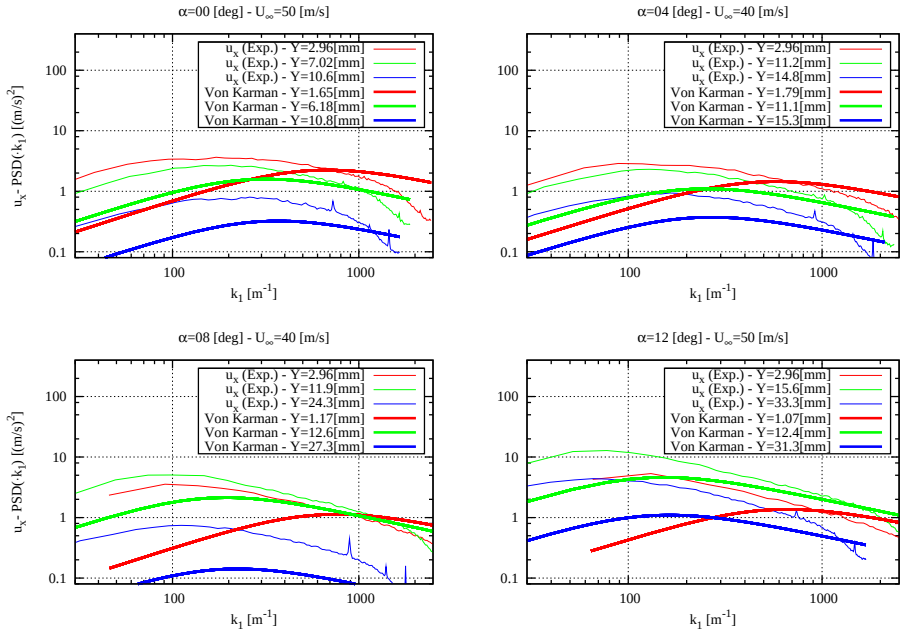

(a) u_x component

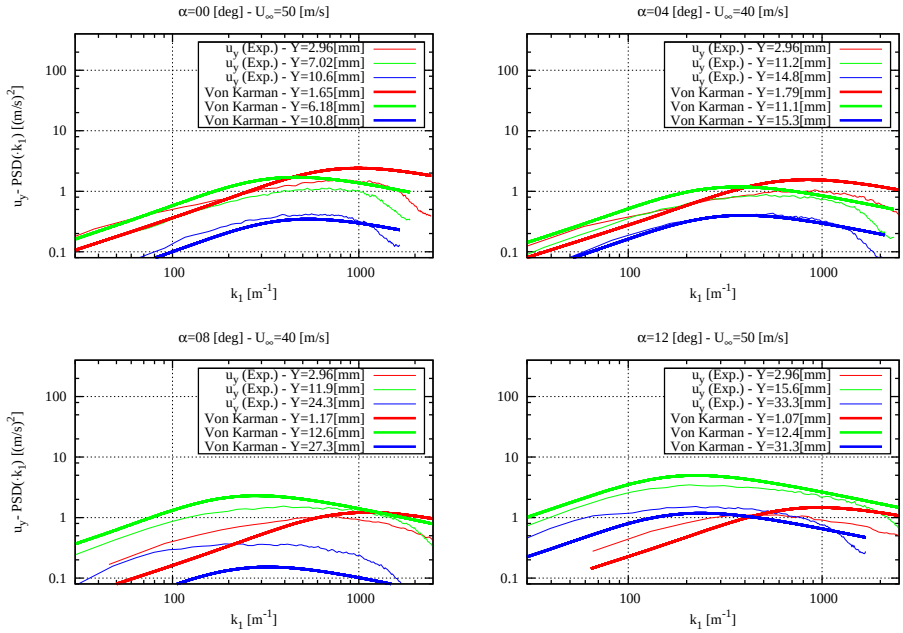

(b) u_y component

Figure 20. Pre-multiplied one-point spectra (V.K. using CFD data)

4.4 Comparison with Measurements in the LWT Wind Tunnel at Stuttgart University

A experimental set-up similar to the present campaign was implemented in the Laminar Wind Tunnel (LWT) in Stuttgart (see Kamruzzaman *et al* [12] for details). Both the NACA0012 airfoil and the VTE_kav airfoil were measured at Reynolds numbers equal to $Re = 1.5 \times 10^6$ ($U_\infty = 57\,\mathrm{m/s}$, $C = 0.4\,\mathrm{m}$) and $Re = 3.1 \times 10^6$ ($U_\infty = 60\,\mathrm{m/s}$, $C = 0.8$ m), respectively. Note that both airfoils were tripped at $x/C = 0.05$ on both sides of the airfoil and that transition is forced at that location in the CFD calculations presented in this section.

Comparisons are herein focused on the vertical velocity turbulent stress $< u_y u_y >$, and more importantly since it could not be measured during the present campaign, the vertical integral length scale for the vertical velocity fluctuations L_2, both of which are main parameters in the TNO model formulation (see Appendix D).

Vertical Velocity Fluctuations

Vertical velocity fluctuations measured for the NACA0012 at angles of attack $\alpha = 0, 2$ and 4^o are compared with the CFD results in Fig. 21(a). In this figure, the vertical velocity turbulent stresses are evaluated using the computed TKE k_T and the original TNO model assumption as in Eq. (D.21):

$$< u_y u_y > = \beta\, k_T$$

where $\beta = 0.45$ is an experimentally tuned factor (see Appendix D). It is obvious that this approximation underestimates the measured turbulent stress values. In Fig.21(b), modified factors different for each angle of attack are used in order to better fit the measurements, namely $\beta = 0.48, 0.52$ and 0.55 for $\alpha = 0, 2$ and 4^o, respectively.

The vertical turbulent stress measured in the LWT wind tunnel for the VTE_kav airfoil are presented next in Fig. 22. The angle of attack is equal to $\alpha = 3.3^o$, which corresponds to a lift coefficient $C_l = 0.7$. The CFD/TNO results are displayed for three different values of the factor β: the isotropic case $\beta = 2/3$, the original TNO model value $\beta = 0.45$, and finally $\beta = 0.55$ which better fits the experimental data.

A similar comparison can be performed for the measurements obtained during the present campaign with the NACA0015 airfoil. The vertical turbulent stresses already used in Section 4.1 are displayed in Fig. 23. However, in this figure, the original TNO model factor $\beta = 0.45$ is used (instead of the isotropic assumption). The comparison model vs. measurements shows a different trend from what is observed in the LWT wind tunnel. It turns out than in the present case, the original model approximation using the factor $\beta = 0.45$ yields a good agreeement at high angles of attack in terms of turbulent stress level, but that this factor should be slightly reduced at lower angles.

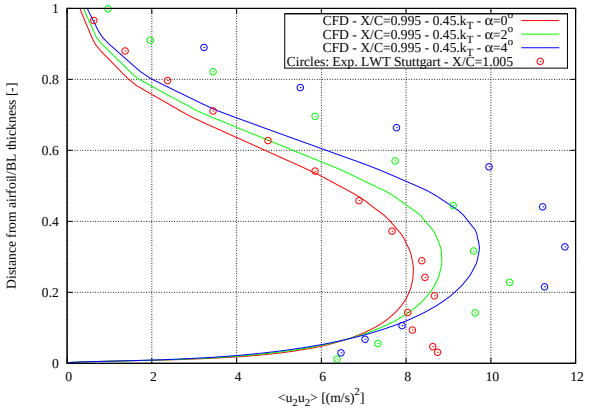

(a) Original TNO model approximation

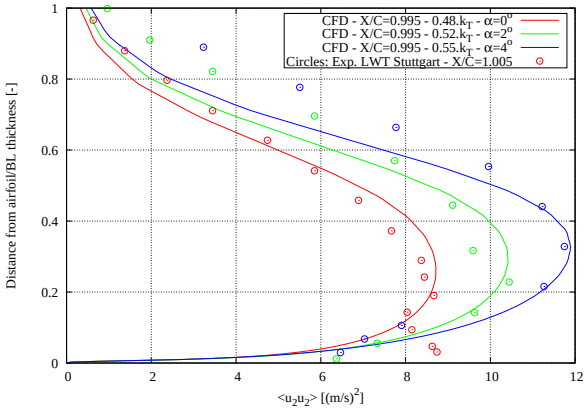

(b) TNO model with modified factors β

Figure 21. Turbulent stress $<u_2u_2>$ near trailing edge - Comparison CFD/TNO vs. LWT measurements - NACA0012 airfoil

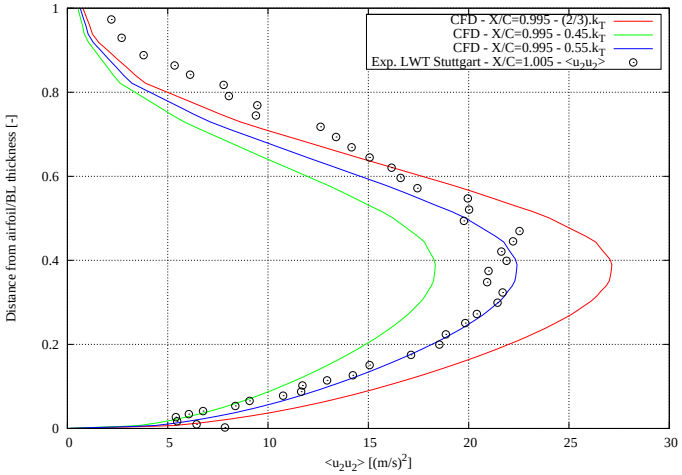

Figure 22. Turbulent stress $<u_2u_2>$ near trailing edge - Comparison CFD/TNO vs. LWT measurements - VTE_kav airfoil

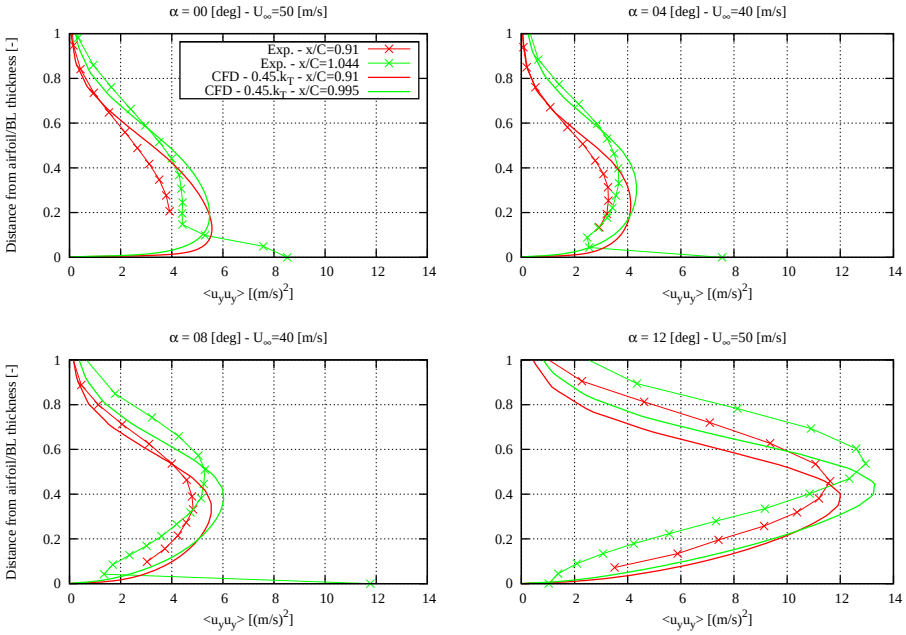

Figure 23. Turbulent stress $<u_2u_2>$ near trailing edge - Comparison CFD/TNO vs. present measurements - NACA0015 airfoil

Vertical Turbulent Length Scale

The vertical turbulent length scale L_2 was also measured in the LWT wind tunnel. Results obtained for the NACA0012 airfoil are displayed in Fig. 25, together with the results from CFD calculations using the original TNO model approximation from Eq. (D.22) (see Appendix D). It can be observed that the model has a tendency to underestimate L_2 as the wall surface is approached.

To correct this discrepancy, the model equation (D.22) is multiplied by a corrective function depending on the normalized distance to the wall defined as:

$$f_c(y/\delta) = 1.0 + 1.3\,(y/\delta)^{1/5}\,\mathrm{e}^{-30\,(y/\delta)^2}$$

where y is the distance to the wall across the BL and δ is the BL thickness. This function is plotted in Fig. 24. The constants in the above formula have been tuned so that the resulting integral length scale better fits the measurements. The corrected formula for the integral length scale then reads:

$$L_{2c} = 0.387\,\frac{k_T^{3/2}}{\epsilon}\,f_c(y/\delta)$$

The results are displayed in Fig. 25. It can be seen that the rapid growth of the integral length scale near the wall surface is better captured by the corrected L_{2c}.

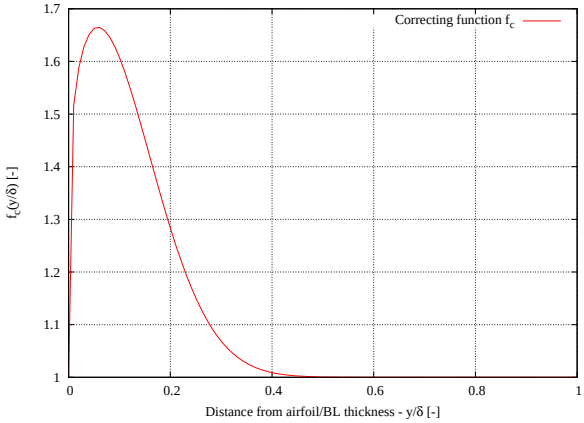

Figure 24. Corrective function for the integral length scale L_{2c}

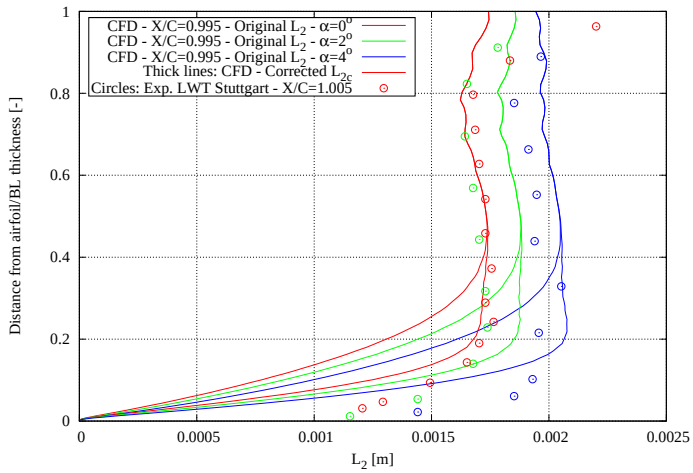

Figure 25. Integral length scale L_2 near trailing edge - Comparison CFD/TNO vs. LWT measurements - NACA0012 airfoil

Results obtained for the VTE_kav airfoil are displayed in Fig. 26. Two sets of experimental data are plotted: one using two hot-wires for measuring the integral length scale L_2, the other using split-film sensors. The CFD model results include the original TNO model approximation and the corrected one as described above. It can be observed that the overall level of the integral length scale across the BL is underestimated by the model and that the corrective function somehow improves the results near the wall surface, though this correction is a bit excessive as a seemingly unphysical large peak occurs around $y/\delta = 0.2$.

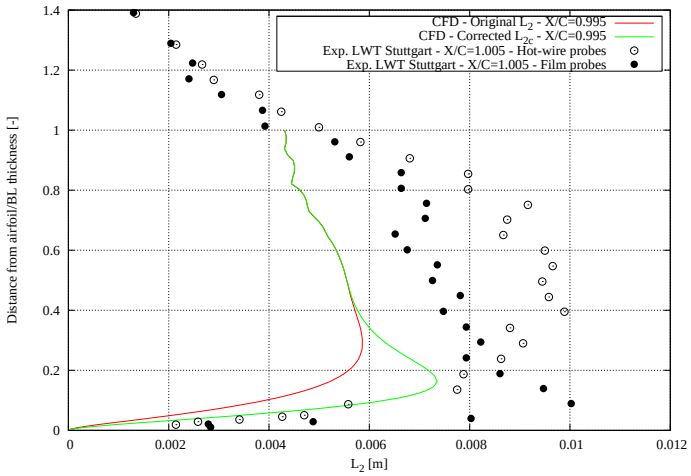

Figure 26. Integral length scale L_2 near trailing edge - Comparison CFD/TNO vs. LWT measurements - VTE_kav airfoil

4.5 Surface Pressure and CFD/TNO Model

As described in Appendix D, the TNO model gives access to the surface pressure fluctuations spectra. These spectra could be reliably measured during the present campaign. In this section, both sets of data are compared at the chord location $X/C = 0.894$. Note that all input flow data for the TNO model have been obtained with CFD calculations (see Appendix D for details). In these calculations, the transition is determined with the e^n transition model by Drela and Giles [8] and the parameter N_{crit} is set to 9. Different versions of the TNO model are compared, including various model parameter values.

Original TNO Model and General Spectral Form

The surface pressure spectra obtained with the original CFD/TNO model are compared with the measurements at the chord location $X/C = 0.894$ in Fig. 27(a). Each of the four subfigures corresponds to one of the considered angles of attack $\alpha = 0, 4, 8$ and 12^o. In each subfigure, results for the three wind tunnel inflow velocities are plotted. It can be observed that the surface pressure is consistently underestimated by the model, and that this underestimation is increasing as the angle of attack increases. However, the form of the measured spectra is quite well predicted by the model. Indeed, the evolution of the spectra (i.e. the spectrum slope at higher frequencies and the spectrum peak frequency) as a function of the angle of attack is very well reproduced by the model, as well as the increasing spectral intensity as a function of the inflow velocity.

In Appendix C.3, a more general spectral functional form for the TKE spectrum than the classical Von Karman spectrum is introduced. This more general form model includes two model parameters n_E and c_E that can be adjusted.

Fig. 27(b) displays the results obtained with the general form model for which the parameter n_E is set to 2. The results are significantly improved for the lowest angle of attack $\alpha = 0^o$. However, as the angle of attack increases, the underestimation of the pressure spectrum reappears at higher frequencies, though the model still performs better at lower frequencies (i.e. around the spectrum peak frequency).

The influence of the parameter c_E is investigated next. Setting its value to 0.5 yields somehow the same effects as above for the n_E parameter, as it can be seen in Fig. 27(c).

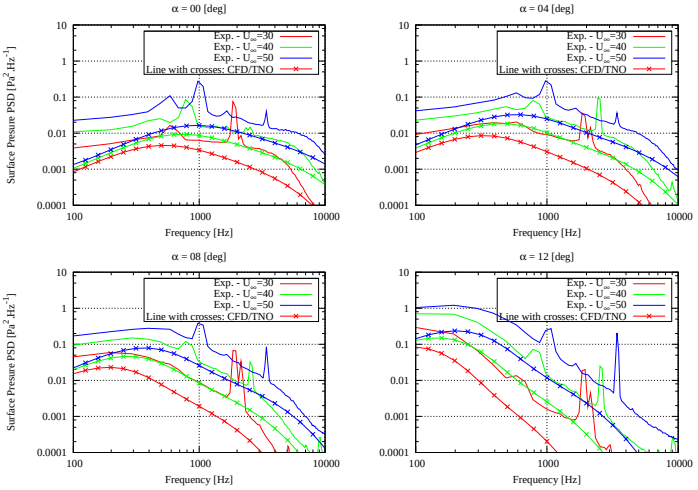

(a) Original CFD/TNO model

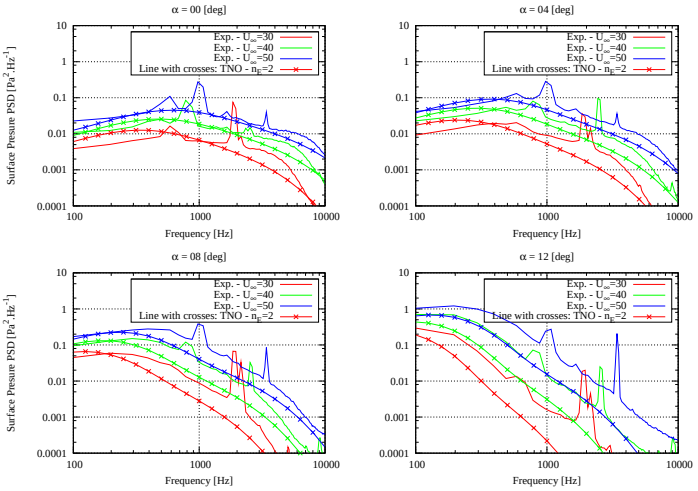

(b) CFD/TNO model - General spectral form - $n_E = 2$

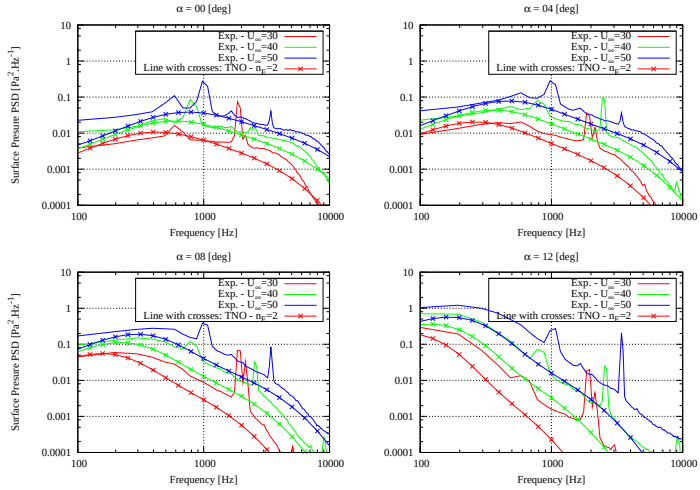

(c) CFD/TNO model - General spectral form - $c_E = 0.5$

Figure 27. Surface pressure at $X/C = 0.894$ - Comparison CFD/TNO vs. experiment

Modified Factor β and Modified k_T

In Section 4.4, it is shown that the factor β used to evaluate the vertical turbulent stress in Eq. (D.21) should be increased to better fit the data measured in the LWT wind tunnel. Here, the modified factor $\beta = 0.55$ is used in the CFD/TNO model to calculate this turbulent stress and subsequently the surface pressure spectra. The results are plotted in Fig. 28(a). It can be seen that there is only a very little improvement compared to the original model in Fig. 27(a).

A second different modification is now applied to the CFD/TNO model. The TKE k_T computed by the CFD code is multiplied by a factor 1.2 before being used as an input for the TNO model. The original factor $\beta = 0.45$ is used. Note that the previous modification not only changes the resulting vertical turbulent stress in the model, but also the calculation of the vertical integral length scale through Eq. (D.22). As it can be seen in Fig. 28(b), the results are greatly improved for the lower angles of attack, but the surface pressure underestimation by the model reappears at $\alpha = 12^o$, and to a lesser extent at 8^o.

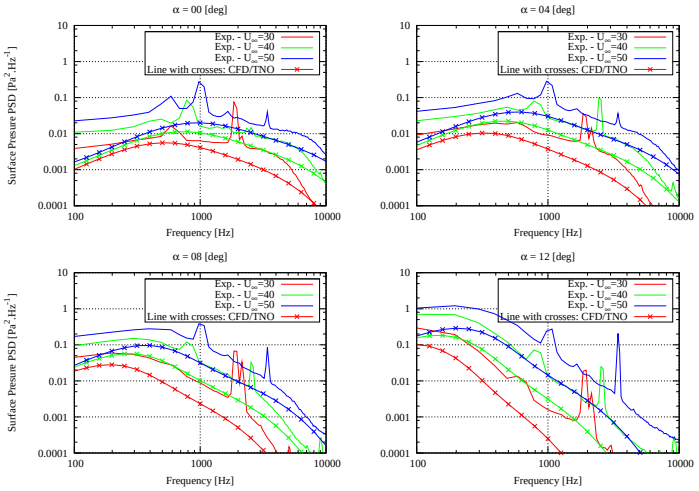

(a) CFD/TNO model - $\beta = 0.55$

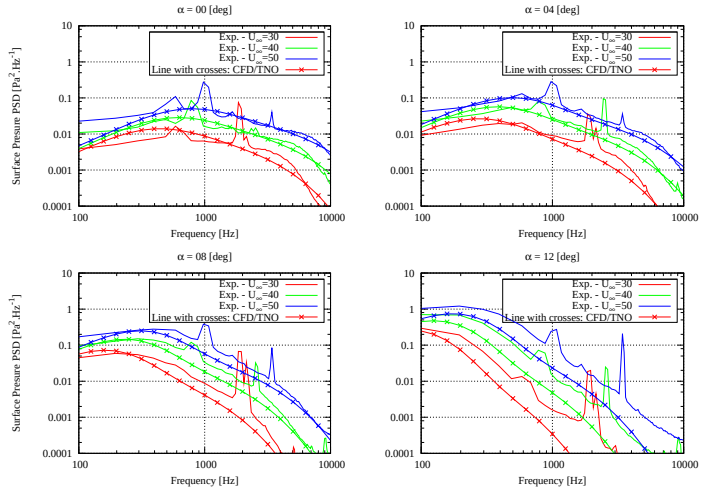

(b) CFD/TNO model - $k_T \rightarrow 1.2\,k_T$

Figure 28. Surface pressure at $X/C = 0.894$ - Comparison CFD/TNO using modified β and k_T vs. experiment

Corrected Integral Length Scale

In Section 4.4, a corrected integral length scale L_{2c} is introduced to account for the discrepancies between the original TNO model approximation of Eq. (D.22) and the integral length scale L_2 measured in the LWT wind tunnel. This corrected integral length scale is used here to calculate the surface pressure spectrum using the CFD/TNO model.

The results are displayed in Fig. 29. It can be seen that the results are significantly improved for the three angles of attack $\alpha = 0, 4$ and 8^o, though a small overestimation is observed at 0^o and an underestimation at 8^o. At 12^o, the large underestimation of the measured surface pressure spectrum by the model reappears.

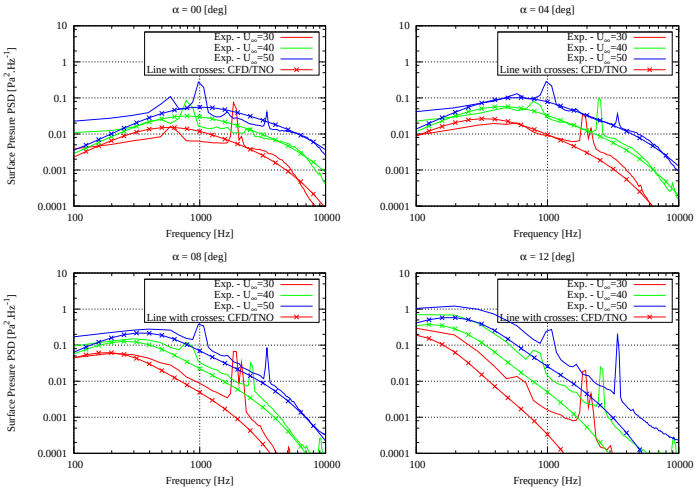

Figure 29. Surface pressure at $X/C = 0.894$ - Comparison CFD/TNO using corrected L_{2c} vs. experiment

4.6 Conclusions

The various tests performed in the previous section to evaluate the impact of the various parameters on the CFD/TNO model prediction of the surface pressure spectra, together with the comparisons of CFD results with BL measurements provide some indications on how to improve the TNO model.

It seems clear from Section 4.1 that the CFD calculations underestimate the TKE in the turbulent BL when the angle of attack is getting large, and that transition alone cannot explain these discrepancies (Section 4.2). This underestimation is increasing as the angle of attack is increasing, which is correlated to the fact that the CFD/TNO model underestimates the surface pressure spectra as the angle of attack increases. However, attempts to increase the TKE (within sensible limits) were not successfull in reducing the discrepancies between measured and modeled surface pressure spectra at high angles of attack.

The main unknown in the calculation of the surface pressure remains the evaluation of vertical integral length scale. It could not be measured with the present experimental set-up but measurements performed at Stuttgart [12] were used for comparison in the present study. Discrepancies could be observed suggesting that the model used in this work may be improved.

5 Trailing Edge Noise Measurements

As described in Section 2, two slanted single hot-wire probes were placed in the wind tunnel near the trailing edge (TE) of the airfoil, one on each side of the TE relatively to the airfoil chord plane. Both probes were located outside of the BL and wake generated by the airfoil itself so that BL/wake turbulence will not affect the measured velocity fluctuations.

The goal is to measure the TE radiated noise that should behave as a dipole and therefore should be characterized as out of phase pressure/velocity fluctuations on both sides of the TE. The slanted probes are orientated so that the hot-wires stand approximately along a line perpendicular to the TE and perpendicular to the line joining the probe to the closest point on the TE. In this way, the set-up will significantly filter out waves that are not parallel to TE noise waves, though waves travelling in the direction parallel to the TE will not be filtered out. One can therefore expect that the resulting measurements will be contaminated by spurious sound waves reflecting on the side walls of the wind tunnel. In any case, it cannot be expected that this set-up will filter out all background noise present in the wind tunnel as it will become clear in the analysis of the measured data below.

Various gains were used to amplify the measured signals in an attempt to increase the signal-to-noise ratio. An analysis of the results that is not presented in this report showed that no significant improvement were obtained by using higher gain values. Results shown in this section are obtained with a gain factor equal to 64. As already mentioned in Section 2, a 100 Hz high-pass filter was applied in order to remove spurious low-frequency fluctuations, together with a 10 kHz low-pass filter to avoid aliasing.

In order to evaluate this measurement technique, three different configurations are investigated here. In the two first ones, the probes are located at approximately 9 cms below and above the plane described by the mean inflow velocity and the TE, and at a distance approximately equal to 13 cms from the TE perpendicularly to the TE direction. In the first case, the angle of attack of the airfoil is equal to $\alpha = 8^o$, and 12^o in the second. As for the third configuration, the probes are located at the same relative locations in the wind tunnel but the airfoil is removed from the wind tunnel.

5.1 Angle of Attack $\alpha = 8^o$

The coherence and phase between the velocities measured by the two hot-wires are plotted in Figs. 30(a) and (b), respectively, for an angle of attack $\alpha = 8^o$ and for the empty wind tunnel at all considered inflow wind speeds $U_\infty = 30, 40$ and 50 m/s. It can be observed that there is no significant difference between the wind tunnel being empty and when the airfoil is present, except at lower frequencies ($f < 600$ Hz) where there exist strong correlated signals captured by the two hot-wires. However, the phase behaviour does not indicate that it is related to TE noise (which should be characterized by a $\pm\pi$ phase shift), but rather that it behaves more like the phase shift of sensors measuring the same traveling wave at different locations (i.e. characterized by a linear variation of the phase as a function of frequency). This latter behaviour could be the result of the two hot-wire probes being located not exactly at the same distance from the acoustic source.

A small frequency range for which the two velocities measured by the hot-wires are out of phase can be observed around $1500 < f < 2100$ Hz. However, it is also observed when the wind tunnel is empty excluding that this could be related to TE noise. In addition, sharp large coherence peaks can be observed above 2000 Hz.

Their frequency locations increase with increasing inflow speed. These are most certainly caused by the wind tunnel fan noise.

The large coherence between the hot-wire signals observed at frequencies lower than approximately 600 Hz is investigated in more detail. The cross-spectra of the two signals are displayed in Fig. 31(a). It is important to note here that, for a sound wave emitted by a dipole source, the velocity is linearly related to the time derivative of the pressure field. Therefore, the velocity amplitude should scale as the pressure amplitude. In addition, the sound wave intensity (proportional to the pressure amplitude squared) of trailing edge noise should scale as U_∞^5 at higher frequencies, i.e. $f \gg c_0/C$ where C is the airfoil chord and c_0 the speed of sound (see Blake [3], Vol.II, p.732), and as U_∞^6 at lower frequencies, i.e. $f \ll c_0/C$. The cross-spectra non-dimensionalized using the two scaling laws are displayed in Figs. 31(b) and (c), respectively. It can be observed that the two scalings give similar results, and that in both cases, the cross-spectra seem to merge into a common curve. In addition, note that the intermediate scaling frequency c_0/C is approximately equal to 380 Hz in our case. This might indicate that the highly correlated signals at low frequencies may originate from a compact acoustic source (low wavenumber acoustic waves relatively to the airfoil chord) due to the interaction of the airfoil with either inflow turbulence or turbulent boundary layer vortices convecting above the trailing edge.

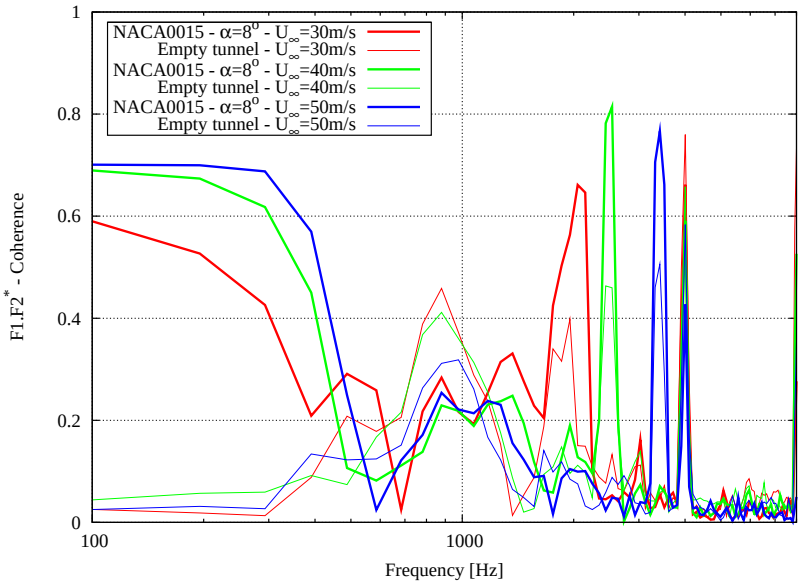

(a) Coherence

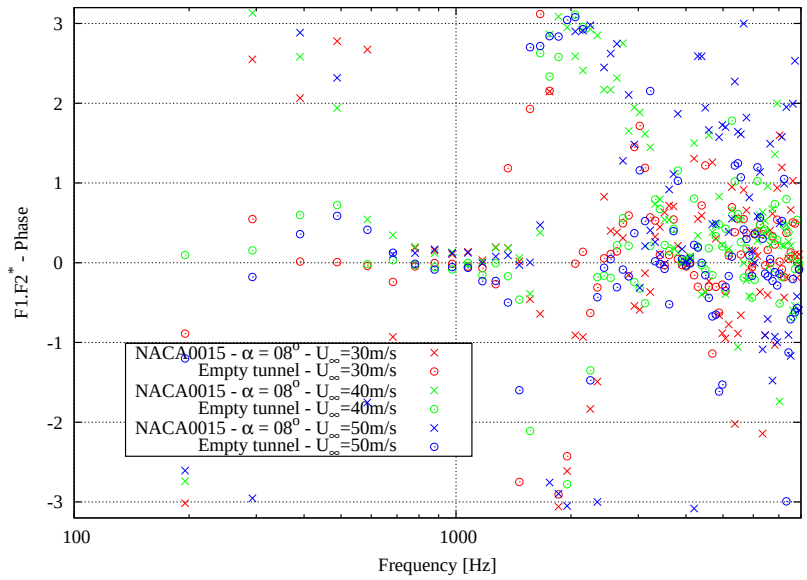

(b) Phase

Figure 30. Coherence/Phase between slanted hot-wire measured velocities - $\alpha = 8^o$ vs. empty wind tunnel

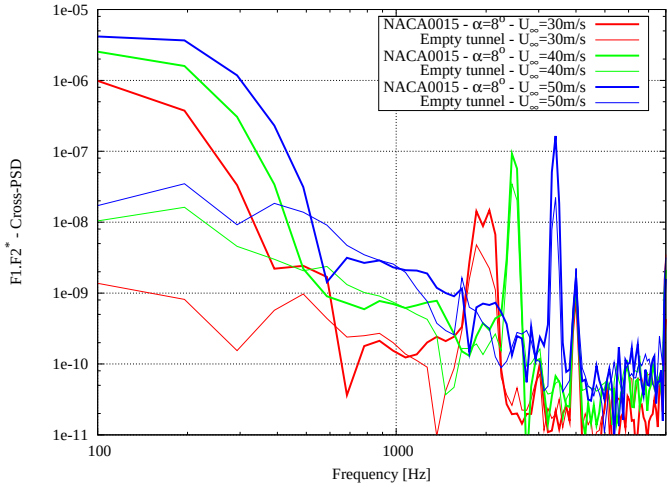

(a) Cross-PSD

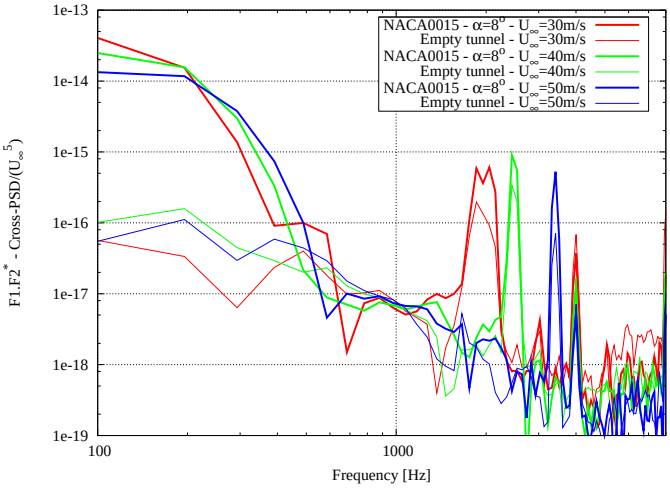

(b) Normalized Cross-PSD (Spectrum normalized by U_∞^5)

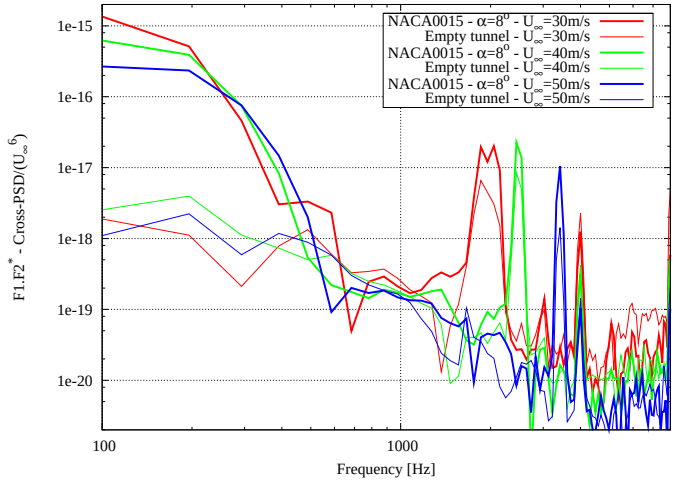

(c) Normalized Cross-PSD (Spectrum normalized by U_∞^6)

Figure 31. Cross-spectra between slanted hot-wire measured velocities - $\alpha = 8^o$ vs. empty wind tunnel

5.2 Angle of Attack $\alpha = 12^o$

The same data as above are displayed for an angle of attack equal to $\alpha = 12^o$ (and the empty tunnel) in Figs. 32(a-b) for the coherence and phase of the two hot-wire measured velocities, and in Figs. 33(a-c) for the cross-spectra. The conclusions are very similar to those of the previous case at $\alpha = 8^o$. However, in the frequency range 2200-3000 Hz, a $\pm\pi$ phase difference can be observed for the inflow velocity $U_\infty = 30$ m/s. It disappears when the wind tunnel is empty, but also when the inflow velocity is increased.

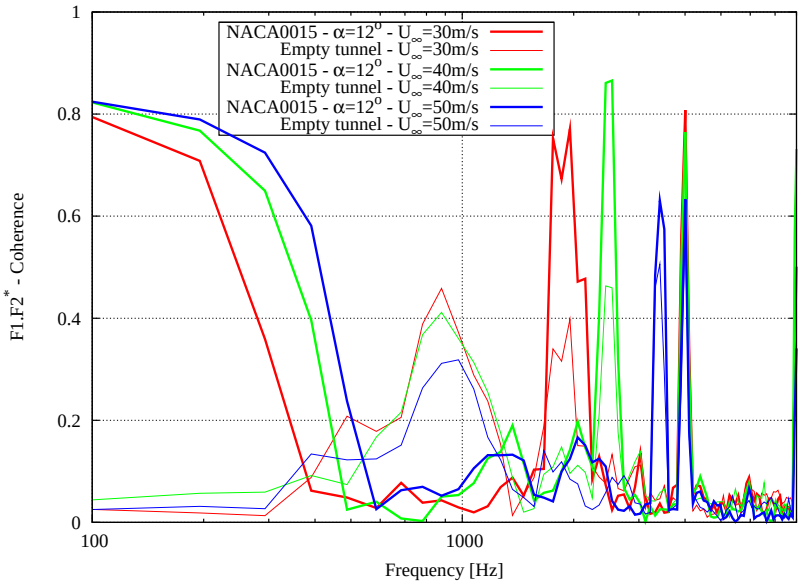

(a) Coherence

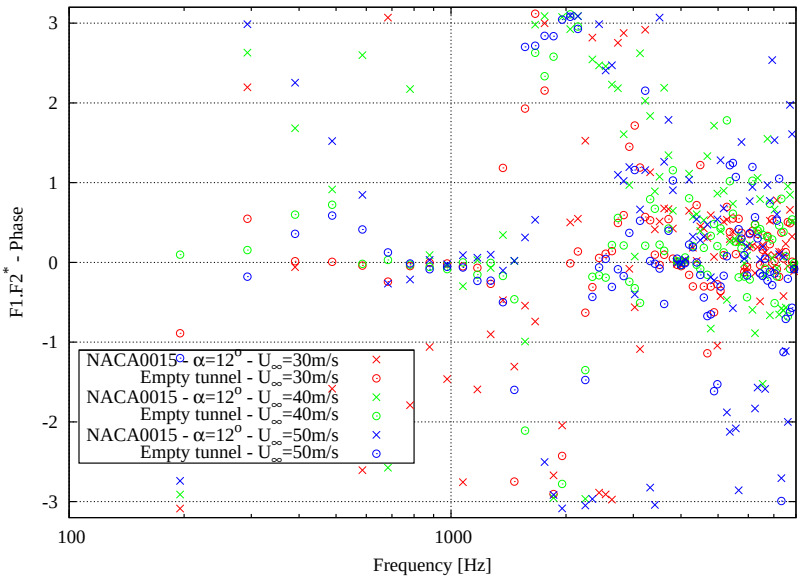

(b) Phase

Figure 32. Coherence/Phase between slanted hot-wire measured velocities - $\alpha = 12^o$ vs. empty wind tunnel

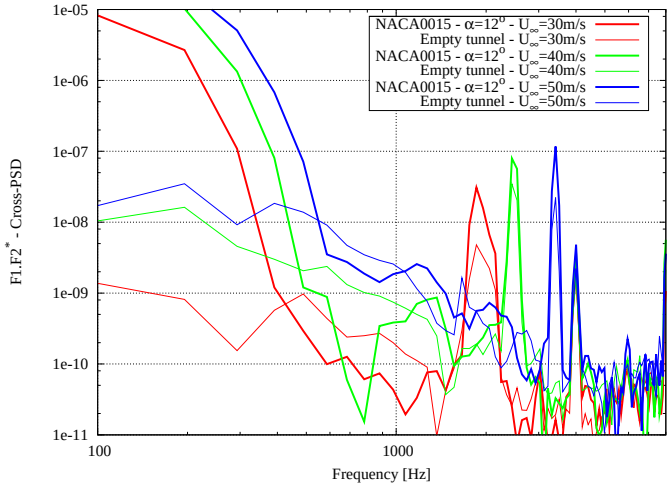

(a) Cross-PSD

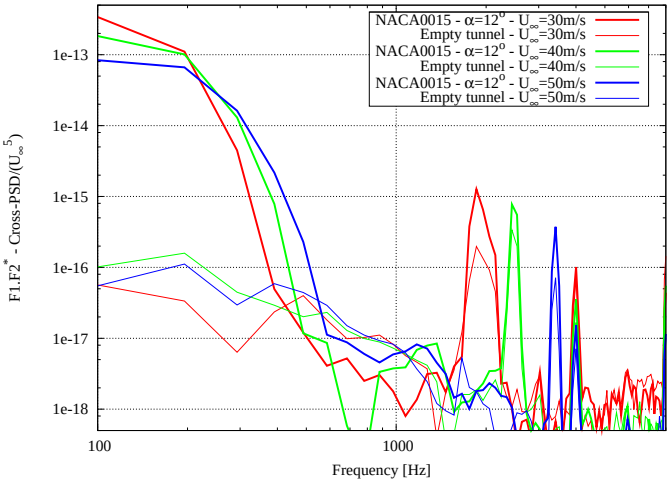

(b) Normalized Cross-PSD (Spectrum normalized by U_∞^5)

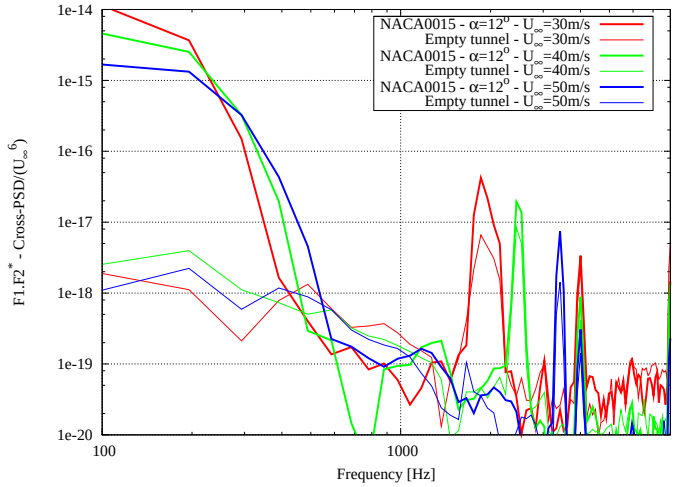

(c) Normalized Cross-PSD (Spectrum normalized by U_∞^6)

Figure 33. Cross-spectra between slanted hot-wire measured velocities - $\alpha = 12^o$ vs. empty wind tunnel

5.3 Conclusions

As a conclusion for this section, it seems that measuring trailing edge noise with the present set-up is not feasible. Some noise related to the presence of the airfoil could be measured at lower frequencies, however, it remains uncertain what its origin is. The main reason for these inconclusive results is most probably the presence of intense background noise which overwhelms the TE noise that we are trying to measure.

6 Conclusion

Hot-wires and surface pressure measurements of the NACA0015 airfoil that were performed in the LM wind tunnel provide a detailed description of the BL mean velocity profiles as well as BL turbulent velocity fluctuations and the associated surface pressure fluctuations. These measurements are intended to validate both the CFD calculations using the RANS code EllipSys2D and the TNO model which uses the previous calculations as an input for the evaluation of the surface pressure spectrum, and subsequently the trailing edge far-field noise. There is a relative quite good agreement between the CFD results and the measurements. Some discrepancies were observed for the turbulent kinetic energy and integral length scale distributions across the boundary layer. The TNO model predicts the qualitative features of the surface pressure as a function of inflow velocity and angle of attack quite well. However, discrepancies exists concerning the quantitative results. In particular, the modeled surface pressure spectra largely underestimate the measurements. Some corrections based on the discrepancies observed between the CFD results and the measured turbulent boundary layer quantities were implemented to improve the model. However, it proved unable to eliminate the surface pressure spectra underestimation at high angles of attack.

The second part of the experiment intended to measure trailing edge noise with hot-wire anemometry. It turns out that the background noise present in the wind tunnel (originating from the fan, boundary layer along the walls of the wind tunnel, reflecting sound waves on these walls, etc...) seems to dominate the whole frequency range where trailing edge noise should be observed. These spurious sound waves could not be filtered out. Nevertheless, sound waves related to the presence of the airfoil could be observed in the frequency range 100-600 Hz. However, their origin could not be clearly identified.

As a final conclusion, it seems that the LM wind tunnel is not adapted to measure trailing edge noise using hot-wire anemometry due to the high background noise present in the tunnel. However, the relative good agreement between the TNO modeled and the measured surface pressure using the flush-mounted airfoil microphones can indirectly give access the radiated trailing edge noise using the TNO model theory.

Acknowledgments

The work presented in this report is funded by the Danish Energy Agency (Energistyrelsen) through the EUDP-project 'Low Noise Airfoil', Journalnr.: 64009-0272.

This experimental campaign would not have been possible without the wind tunnel facility provided by LM Wind Power and its Senior Manager Aerodynamics Peter Fuglsang, as well as the help of Olaf, Kenny and Hans.

The measurements were performed using a traverse system and probe holders that were designed and which manufacturing was supervised by Andreas Fischer. Therefore, even if he could not be present during the campaign, it is mainly thanks to him that the hot-wire measurements could be performed successfully.

Finally, the author would like to thank DTU-MEK/Robert Michelsen for providing access to the jet facility that was used to calibrate the hot-wire sensors.

References

[1] G. K. Batchelor, *The Theory of Homogeneous Turbulence*, vol. in Applied Mathematics and Mechanics, Cambridge University Press, Cambridge (UK), 1953.

[2] F. Bertagnolio, *NACA0015 Measurements in LM Wind Tunnel and Turbulence Generated Noise*, Tech. Rep. Risø-R-1657(EN), Risø-DTU, Roskilde, Denmark, November 2008.

[3] W. K. Blake, *Mechanics of Flow-Induced Sound and Vibration, Vol.I and II*, vol. in Applied Mathematics and Mechanics, Frenkiel, F.N. and Temple, G. (eds.), Academic Press, 1986.

[4] T. F. Brooks and T. H. Hodgson, *Trailing Edge Noise Prediction from Measured Surface Pressures*, J. Sound Vib. **78** (1981), no. 1, 69–117.

[5] D.M. Chase, *Noise Radiated from an Edge in Turbulent Flow*, AIAA J. **13** (1975), no. 8, 1041–1047.

[6] M. Døssing, *High Frequency Microphone Measurements for Transition Detection on Airfoils*, Tech. Rep. Risø-R-1645(EN), Risø-DTU, Roskilde, Denmark, June 2008.

[7] M. Drela, *Low Reynolds Number Aerodynamics*, vol. 54, ch. XFOIL: An Analysis and Design System for Low Reynolds Number Airfoils, pp. 1–12, Mueller, T.J. (ed.), Lecture Notes in Engineering, Springer-Verlag, Berlin, 1989.

[8] M. Drela and M. B. Giles, *Viscous-Inviscid Analysis of Transonic and Low Reynolds Number Airfoils*, AIAA Journal **25** (1987), no. 10, 1347–1355.

[9] A. Fischer, F. Bertagnolio, C. Bak, and H. Aa. Madsen, *Surface Pressure Measurements on a NACA0015 airfoil compared to Computations with the TNO Trailing Edge Noise Model*, Proc. of the Torque 2010 'The science of making torque from wind' Conf. (EWEA) (Heraklion, GR), June 2010, pp. 81–92.

[10] J. O. Hinze, *Turbulence*, McGraw Hill, 1959.

[11] F. E. Jørgensen, *How to Measure Turbulence with Hot-Wire Anemometer - A Practical Guide*, Available at: http://www.dantecdynamics.com/Admin/Public, 2002.

[12] M. Kamruzzaman, T. Lutz, A. Herrig, and E. Krämer, *RANS Based Prediction of Airfoil Trailing Edge Far-Field Noise: Impact of Isotropic & Anisotropic Turbulence*, Proc. of the 14^{th} AIAA/CEAS Aeroacoustics Conf. (Vancouver), AIAA Paper 2008-2867, 2008.

[13] J. L. Lumley, *Stochastic Tools in Turbulence*, Academic Press, 1970.

[14] T. Lutz, A. Herrig, W. Würz, M. Kamruzzaman, and E. Krämer, *Design and Wind-Tunnel Verification of Low-Noise Airfoils for Wind Turbines*, AIAA Journal **45** (2007), no. 4, 779–785.

[15] J. Mathieu and J. Scott, *Introduction to Turbulent Flow*, Cambridge University Press, Cambridge (UK), 2000.

[16] F. R. Menter, *Zonal Two-Equations k–ω Turbulence Models for Aerodynamic Flows*, Proceedings, AIAA Paper 93-2906, 1993.

[17] J. A. Michelsen, *Basis3D - A Platform for Development of Multiblock PDE Solvers*, Tech. Rep. AFM 92-05, Technical University of Denmark, 1992.

[18] ———, *Block Structured Multigrid Solution of 2D and 3D Elliptic PDE's*, Tech. Rep. AFM 94-06, Technical University of Denmark, 1994.

[19] H. D. Papenfuß, *Aerodynamic Commissioning of the New Wind Tunnel at LM Glasfiber A/S (Lunderskov); Private Communication*, Property of LM Glasfiber, June 2006.

[20] R. Parchen, *Progress report DRAW: A Prediction Scheme for Trailing-Edge Noise Based on Detailed Boundary-Layer Characteristics*, TNO Rept. HAG-RPT-980023, TNO Institute of Applied Physics, The Netherlands, 1998.

[21] H. Schlichting, *Boundary Layer Theory*, McGraw Hill, 1968.

[22] N. N. Sørensen, *General Purpose Flow Solver Applied to Flow over Hills*, Risø-R-827-(EN), Risø National Laboratory, Roskilde, Denmark, June 1995.

[23] S. Wagner, G. Guidati, and J. Ostertag, *Numerical Simulation of the Aerodynamics and Acoustics of Horizontal Axis Wind Turbines*, Proc. of the 4^{th} European Conp. Fluid Dyn. Conf. (ECCOMAS) (Athens (GR)) (Papailiou, K. (ed.), ed.), vol. Vol.2, 1998, pp. 436–441.

A Boundary Layer Measurement Points Distributions

During the measurement campaign, different types of measurement 'series' were performed (see Section 2.4). In addition to their respective experimental conditions, each series differs by the number of points measured across the boundary layer (BL) when the hot-wire probe is translated perpendicularly to the airfoil chord, as well as by the distribution of these points across the BL. Furthermore, this distribution is different for each considered angle of attack considered in order to account for the thickening of the turbulent BL as the angle of attack increases.

There exists three types of such distributions denoted as:

- 'Original': contains 24 points - 16/8 points on the suction/pressure side (see table in Fig. 34)
- 'Extended': contains 16 points - all on the suction side (see table in Fig. 35)
- 'DBL': contains 10 points - all on the suction side (see table in Fig. 36)

Note that the series S03 is using the 'Original' distribution set, but only the 16 points on the suction are actually measured. This is due to the fact that for this series, the probe is located upstream of the trailing edge and measuring on the pressure side as well would have required to manually change the set-up at each measured velocity and angle of attack or alternatively perform each case at different times, which is cumbersome.

In the above-mentioned figures, the first column in the tables provides a record number. Each record corresponds to a time-series acquired at a specific location across the BL and those are stored consecutively in a file of the database. Note that *when both the pressure and suction sides are explored*, which only occur for the 'Original' distribution set, the hot-wire probe is first positioned at the point the furthest away on the pressure side (Record No.24 in the table) and moved step by step towards the airfoil trailing edge (Record No.17). Then, it is going over to the suction side at the level of the trailing edge (Record No.1) and continues away from the airfoil towards the point with Record No.16. *When only the suction side is explored*, the hot-wire probe is moved from the point closest to the airfoil (Record No.1) towards the one the furthest away (Record No.16 or No.10 for the 'DBL' distribution set).

The second column gives the actual distance travelled by the hot-wire probe from its initial location (i.e. record No.1). Note that in the figures displayed in this report, firstly an offset (see below) has been added to this value, secondly it has been multiplied by $\cos(\theta)$, θ being the angle between the normal to the wall and the normal to the airfoil chord axis (or equivalently between the airfoil surface and the airfoil chord axis), so that the resulting plotted value is approximately the distance from the probe to the airfoil surface along the normal to the wall. The angles that are used at the various chordwise locations where data are displayed in this report are given in Table 2. Note that when displaying profiles downstream of the trailing edge, the same angle as for the last chordwise position ($X/C = 0.995$) is used. The second of the above manipulations is due to the fact that the traverse system holding the probe is moving along the normal to the chord axis, but results from CFD calculations are obtained as a function of the distance to the wall along the surface normal. Indeed, the CFD results are subsequently used in the TNO noise model which is based on the flow above a flat plate, and it is therefore more natural to project the results on the normal to the airfoil surface.

X/C	θ [^{o}]
0.91	8.997
0.97	9.617
0.995	9.895

Table 2. Angle between chord axis and airfoil surface

The third column is the step motor position (in number of rotation steps) and should be of no use for the reader.

Above the tables, the distances from the initial point (Record No.1) to the point furthest away from the airfoil are provided, both in meter and normalized by the airfoil chord. Note that for measurements performed directly above the airfoil (i.e. not in the wake: $X/C < 1$), an offset (denoted 'Yref' and given in the table in Fig. 3, Section 2.4) has to be added to the distances specified in the tables presented in this section in order to account for the initial position of the probe (which is obviously slightly above the airfoil wall).

		Delta$_s$/C =	2.35E-02
SUCTION SIDE		Delta$_s$ [m]=	2.12E-02
Record No.	Y/Delta$_s$	Y[m]	Step Pos.
1	0.00	0.00E+00	0.0
2	0.04	8.46E-04	-75.7
3	0.08	1.69E-03	-151.3
4	0.12	2.54E-03	-227.0
5	0.16	3.38E-03	-302.7
6	0.20	4.23E-03	-378.4
7	0.25	5.29E-03	-472.9
8	0.30	6.35E-03	-567.5
9	0.36	7.61E-03	-681.0
10	0.42	8.88E-03	-794.5
11	0.48	1.02E-02	-908.1
12	0.54	1.14E-02	-1021.6
13	0.62	1.31E-02	-1172.9
14	0.70	1.48E-02	-1324.2
15	0.80	1.69E-02	-1513.4
16	1.00	2.12E-02	-1891.8
		Delta$_p$/C =	2.35E-02
PRESSURE SIDE		Delta$_p$ [m]=	2.12E-02
Record No.	Y/Delta$_p$	Y[m]	Step Pos.
Not a record	0.00	0.00E+00	0.0
17	-0.08	-1.69E-03	151.3
18	-0.16	-3.38E-03	302.7
19	-0.25	-5.29E-03	472.9
20	-0.35	-7.40E-03	662.1
21	-0.45	-9.52E-03	851.3
22	-0.60	-1.27E-02	1135.1
23	-0.80	-1.69E-02	1513.4
24	-1.00	-2.12E-02	1891.8

(a) $\alpha = 0^o$

		Delta$_s$/C =	3.20E-02
SUCTION SIDE		Delta$_s$ [m]=	2.88E-02
Record No.	Y/Delta$_s$	Y[m]	Step Pos.
1	0.00	0.00E+00	0.0
2	0.04	1.15E-03	-103.0
3	0.08	2.30E-03	-206.1
4	0.12	3.46E-03	-309.1
5	0.16	4.61E-03	-412.2
6	0.20	5.76E-03	-515.2
7	0.25	7.20E-03	-644.0
8	0.30	8.64E-03	-772.8
9	0.36	1.04E-02	-927.4
10	0.42	1.21E-02	-1081.9
11	0.48	1.38E-02	-1236.5
12	0.54	1.56E-02	-1391.1
13	0.62	1.79E-02	-1597.1
14	0.70	2.02E-02	-1803.2
15	0.80	2.30E-02	-2060.8
16	1.00	2.88E-02	-2576.0
		Delta$_p$/C =	1.60E-02
PRESSURE SIDE		Delta$_p$ [m]=	1.44E-02
Record No.	Y/Delta$_p$	Y[m]	Step Pos.
Not a record	0.00	0.00E+00	0.0
17	-0.08	-1.15E-03	103.0
18	-0.16	-2.30E-03	206.1
19	-0.25	-3.60E-03	322.0
20	-0.35	-5.04E-03	450.8
21	-0.45	-6.48E-03	579.6
22	-0.60	-8.64E-03	772.8
23	-0.80	-1.15E-02	1030.4
24	-1.00	-1.44E-02	1288.0

(b) $\alpha = 4^o$

		Delta$_s$/C =	4.50E-02
SUCTION SIDE		Delta$_s$ [m]=	4.05E-02
Record No.	Y/Delta$_s$	Y[m]	Step Pos.
1	0.00	0.00E+00	0.0
2	0.04	1.62E-03	-144.9
3	0.08	3.24E-03	-289.8
4	0.12	4.86E-03	-434.7
5	0.16	6.48E-03	-579.6
6	0.20	8.10E-03	-724.5
7	0.25	1.01E-02	-905.6
8	0.30	1.22E-02	-1086.8
9	0.36	1.46E-02	-1304.1
10	0.42	1.70E-02	-1521.5
11	0.48	1.94E-02	-1738.8
12	0.54	2.19E-02	-1956.2
13	0.62	2.51E-02	-2246.0
14	0.70	2.84E-02	-2535.8
15	0.80	3.24E-02	-2898.0
16	1.00	4.05E-02	-3622.5
		Delta$_p$/C =	1.10E-02
PRESSURE SIDE		Delta$_p$ [m]=	9.90E-03
Record No.	Y/Delta$_p$	Y[m]	Step Pos.
Not a record	0.00	0.00E+00	0.0
17	-0.08	-7.92E-04	70.8
18	-0.16	-1.58E-03	141.7
19	-0.25	-2.48E-03	221.4
20	-0.35	-3.47E-03	309.9
21	-0.45	-4.46E-03	398.5
22	-0.60	-5.94E-03	531.3
23	-0.80	-7.92E-03	708.4
24	-1.00	-9.90E-03	885.5

(c) $\alpha = 8^o$

		Delta$_s$/C =	6.60E-02
SUCTION SIDE		Delta$_s$ [m]=	5.94E-02
Record No.	Y/Delta$_s$	Y[m]	Step Pos.
1	0.00	0.00E+00	0.0
2	0.04	2.38E-03	-212.5
3	0.08	4.75E-03	-425.0
4	0.12	7.13E-03	-637.6
5	0.16	9.50E-03	-850.1
6	0.20	1.19E-02	-1062.6
7	0.25	1.49E-02	-1328.3
8	0.30	1.78E-02	-1593.9
9	0.36	2.14E-02	-1912.7
10	0.42	2.49E-02	-2231.5
11	0.48	2.85E-02	-2550.3
12	0.54	3.21E-02	-2869.1
13	0.62	3.68E-02	-3294.1
14	0.70	4.16E-02	-3719.1
15	0.80	4.75E-02	-4250.4
16	1.00	5.94E-02	-5313.1
		Delta$_p$/C =	9.50E-03
PRESSURE SIDE		Delta$_p$ [m]=	8.55E-03
Record No.	Y/Delta$_p$	Y[m]	Step Pos.
Not a record	0.00	0.00E+00	0.0
17	-0.08	-6.84E-04	61.2
18	-0.16	-1.37E-03	122.4
19	-0.25	-2.14E-03	191.2
20	-0.35	-2.99E-03	267.7
21	-0.45	-3.85E-03	344.1
22	-0.60	-5.13E-03	458.9
23	-0.80	-6.84E-03	611.8
24	-1.00	-8.55E-03	764.8

(d) $\alpha = 12^o$

Figure 34. Distribution type 'Original'

		Delta$_s$/C =	2.85E-02
SUCTION SIDE		Delta$_s$ [m]=	2.57E-02
Record No.	Y/Delta$_s$	Y[m]	Step Pos.
1	0.00	0.00E+00	0.0
2	0.04	1.03E-03	-91.8
3	0.08	2.05E-03	-183.5
4	0.12	3.08E-03	-275.3
5	0.16	4.10E-03	-367.1
6	0.20	5.13E-03	-458.9
7	0.25	6.41E-03	-573.6
8	0.30	7.70E-03	-688.3
9	0.36	9.23E-03	-825.9
10	0.42	1.08E-02	-963.6
11	0.48	1.23E-02	-1101.3
12	0.54	1.39E-02	-1238.9
13	0.62	1.59E-02	-1422.5
14	0.70	1.80E-02	-1606.0
15	0.80	2.05E-02	-1835.4
16	1.00	2.57E-02	-2294.3

(a) $\alpha = 0^o$

		Delta$_s$/C =	3.70E-02
SUCTION SIDE		Delta$_s$ [m]=	3.33E-02
Record No.	Y/Delta$_s$	Y[m]	Step Pos.
1	0.00	0.00E+00	0.0
2	0.04	1.33E-03	-119.1
3	0.08	2.66E-03	-238.3
4	0.12	4.00E-03	-357.4
5	0.16	5.33E-03	-476.6
6	0.20	6.66E-03	-595.7
7	0.25	8.33E-03	-744.6
8	0.30	9.99E-03	-893.6
9	0.36	1.20E-02	-1072.3
10	0.42	1.40E-02	-1251.0
11	0.48	1.60E-02	-1429.7
12	0.54	1.80E-02	-1608.4
13	0.62	2.06E-02	-1846.7
14	0.70	2.33E-02	-2085.0
15	0.80	2.66E-02	-2382.8
16	1.00	3.33E-02	-2978.5

(b) $\alpha = 4^o$

		Delta$_s$/C =	5.00E-02
SUCTION SIDE		Delta$_s$ [m]=	4.50E-02
Record No.	Y/Delta$_s$	Y[m]	Step Pos.
1	0.00	0.00E+00	0.0
2	0.04	1.80E-03	-161.0
3	0.08	3.60E-03	-322.0
4	0.12	5.40E-03	-483.0
5	0.16	7.20E-03	-644.0
6	0.20	9.00E-03	-805.0
7	0.25	1.13E-02	-1006.3
8	0.30	1.35E-02	-1207.5
9	0.36	1.62E-02	-1449.0
10	0.42	1.89E-02	-1690.5
11	0.48	2.16E-02	-1932.0
12	0.54	2.43E-02	-2173.5
13	0.62	2.79E-02	-2495.5
14	0.70	3.15E-02	-2817.5
15	0.80	3.60E-02	-3220.0
16	1.00	4.50E-02	-4025.0

(c) $\alpha = 8^o$

		Delta$_s$/C =	7.10E-02
SUCTION SIDE		Delta$_s$ [m]=	6.39E-02
Record No.	Y/Delta$_s$	Y[m]	Step Pos.
1	0.00	0.00E+00	0.0
2	0.04	2.56E-03	-228.6
3	0.08	5.11E-03	-457.2
4	0.12	7.67E-03	-685.9
5	0.16	1.02E-02	-914.5
6	0.20	1.28E-02	-1143.1
7	0.25	1.60E-02	-1428.9
8	0.30	1.92E-02	-1714.7
9	0.36	2.30E-02	-2057.6
10	0.42	2.68E-02	-2400.5
11	0.48	3.07E-02	-2743.5
12	0.54	3.45E-02	-3086.4
13	0.62	3.96E-02	-3543.6
14	0.70	4.47E-02	-4000.9
15	0.80	5.11E-02	-4572.5
16	1.00	6.39E-02	-5715.6

(d) $\alpha = 12^o$

Figure 35. Distribution type 'Extended'

		Delta$_s$/C =	3.00E-02
SUCTION SIDE		Delta$_s$ [m]=	2.70E-02
Record No.	Y/Delta$_s$	Y[m]	Step Pos.
1	0.00	0.00E+00	0.0
2	0.15	4.05E-03	-362.3
3	0.30	8.10E-03	-724.5
4	0.40	1.08E-02	-966.0
5	0.50	1.35E-02	-1207.5
6	0.60	1.62E-02	-1449.0
7	0.70	1.89E-02	-1690.5
8	0.80	2.16E-02	-1932.0
9	0.90	2.43E-02	-2173.5
10	1.00	2.70E-02	-2415.0

(a) $\alpha = 0^o$

		Delta$_s$/C =	4.30E-02
SUCTION SIDE		Delta$_s$ [m]=	3.87E-02
Record No.	Y/Delta$_s$	Y[m]	Step Pos.
1	0.00	0.00E+00	0.0
2	0.15	5.81E-03	-519.2
3	0.30	1.16E-02	-1038.5
4	0.40	1.55E-02	-1384.6
5	0.50	1.94E-02	-1730.8
6	0.60	2.32E-02	-2076.9
7	0.70	2.71E-02	-2423.1
8	0.80	3.10E-02	-2769.2
9	0.90	3.48E-02	-3115.4
10	1.00	3.87E-02	-3461.5

(b) $\alpha = 4^o$

		Delta$_s$/C =	6.40E-02
SUCTION SIDE		Delta$_s$ [m]=	5.76E-02
Record No.	Y/Delta$_s$	Y[m]	Step Pos.
1	0.00	0.00E+00	0.0
2	0.15	8.64E-03	-772.8
3	0.30	1.73E-02	-1545.6
4	0.40	2.30E-02	-2060.8
5	0.50	2.88E-02	-2576.0
6	0.60	3.46E-02	-3091.2
7	0.70	4.03E-02	-3606.4
8	0.80	4.61E-02	-4121.6
9	0.90	5.18E-02	-4636.9
10	1.00	5.76E-02	-5152.1

(c) $\alpha = 8^o$

		Delta$_s$/C =	8.00E-02
SUCTION SIDE		Delta$_s$ [m]=	7.20E-02
Record No.	Y/Delta$_s$	Y[m]	Step Pos.
1	0.00	0.00E+00	0.0
2	0.15	1.08E-02	-966.0
3	0.30	2.16E-02	-1932.0
4	0.40	2.88E-02	-2576.0
5	0.50	3.60E-02	-3220.0
6	0.60	4.32E-02	-3864.0
7	0.70	5.04E-02	-4508.1
8	0.80	5.76E-02	-5152.1
9	0.90	6.48E-02	-5796.1
10	1.00	7.20E-02	-6440.1

(d) $\alpha = 12^o$

Figure 36. Distribution type 'DBL'

B Hot-Wire Calibration and Voltage to Velocity Transformation

Various single-wire and bi-axial sensor probes designed for the measurements of turbulent velocity components were purchased from Dantec Dynamics for this campaign (see the user guide for details about the probes, their calibration and voltage to velocity transformation [11]).

Although the accompanying acquisition software StreamWare also performs calibration and analysis of the raw measurements data, it is decided here to implement the calibration and analysis with an in-house Fortran code. Indeed, some bugs or misuse of the software lead to corrupted results in some cases. The details of the code implementation are reported here.

Temperature Correction

As mentioned in Section 2, the temperature in the wind tunnel was not kept constant. Before any further treament of the measured voltages, a temperature correction is applied to the data. If E is a raw voltage and T the temperature at which it was measured, the raw voltage is corrected by a multiplicative factor as:

$$E_c = E \cdot \left(\frac{T_\mathrm{w} - T_\mathrm{ref}}{T_\mathrm{w} - T} \right)^{m^*}$$

where the exponent m^* is calculated as:

$$m^* = \begin{cases} (1+m)/2 & \text{if } T > T_\mathrm{ref} \\ (1-m)/2 & \text{otherwise} \end{cases}$$

The loading factor m is characteristic of the fluid and is here taken as $m = 0.2$. In the above formula, T_ref is the reference temperature at which the hot-wire was calibrated. T_w is the sensor hot-temperature which is calculated as:

$$T_\mathrm{w} = T_\mathrm{ref} + \frac{R}{T_\mathrm{cr20} / \big(1 + T_\mathrm{cr20}(T_\mathrm{ref} - 20)\big)}$$

where R is the overheat ratio of the resistance bridge controlling the hot-wire and T_cr20 is the sensor temperature coefficient of resistance at 20^{o}C. These values are given by the manufacturer:

$$R = 0.8 \qquad \text{and} \qquad T_\mathrm{cr20} = 0.36\%$$

Note that the temperature correction has rather small effects on the results in our case.

Calibration

Measurements for each of the wires/sensors (3, 2 or 1 depending on the probe type) provide a voltage E (in Volts) that can be related to a calibration inflow velocity U_{cal} (in m/s) through the following 4^{th} order polynomial approximation:

$$U_{cal} = C_0 + C_1 \cdot E + C_2 \cdot E^2 + C_3 \cdot E^3 + C_4 \cdot E^4$$

where the C_i coefficients are calibration constants to be defined. In our case, these coefficients are optimized to best fit a series of calibration velocities/voltages obtained in a jet. The resulting calibration polynomial should not be used outside of this velocity range as it may oscillate. Note that the calibration voltages have to be corrected for temperature before determining the calibration coefficients.

For velocities outside the calibration range, it is safer to use King's law:

$$U_{cal} = (A_0 + A_1 \cdot E^2)^{A_3}$$

where the A_i coefficients are optimized to best fit the lower or higher part of the calibration curve. A_3 should be close to 1/2.

A smooth interpolation is used as transition between the two previous approximations.

The previous analysis is performed for each of the probe sensors and results in one set of calibration constants for each wire of the probe. This yields three calibration velocities $\{U_{cal1}, U_{cal2}, U_{cal3}\}$ for any set of measured raw voltages for a three-wires probe, only two for a X-wires probe, and one for a single-wire probe. In the latter case (single-wire), not further transformation is needed.

Coordinates Transformation for Tri-axial Probe

In the case of a three-wires probe, the wind speed velocities in the wire-coordinates system $\{U_1, U_2, U_3\}$ are then calculated by inverting the following 3×3 matrix:

$$\begin{aligned}
k_1^2\cdot U_1^2 + \quad U_2^2 + h_1^2\cdot U_3^2 &= (1+k_1^2+h_1^2)\cdot\cos^2(54.74^o)\cdot U_{cal1}^2\\
h_2^2\cdot U_1^2 + k_2^2\cdot U_2^2 + \quad U_3^2 &= (1+k_2^2+h_2^2)\cdot\cos^2(54.74^o)\cdot U_{cal2}^2\\
U_1^2 + h_3^2\cdot U_2^2 + k_3^2\cdot U_3^2 &= (1+k_3^2+h_3^2)\cdot\cos^2(54.74^o)\cdot U_{cal3}^2
\end{aligned}$$

Note that there is a typing error in the formula given in the user guide report provided by Dantec Dynamics [11], p.31. The conductivity-related coefficients are provided by the manufacturer:

$$k_i^2 = k^2 = 0.04 \quad \text{and} \quad h_i^2 = h^2 = 1.20 \qquad (i = 1,2,3)$$

Finally, the velocity components in the probe-coordinates system $\{U, V, W\}$ can be deduced from the previously calculated values as:

$$\begin{aligned}
U = &+\cos(54.74^o)\cdot U_1 + \cos(54.74^o)\cdot U_2 + \cos(54.74^o)\cdot U_3\\
V = &-\cos(45.0^o)\cdot U_1 - \cos(135.0^o)\cdot U_2 + \cos(90.0^o)\cdot U_3\\
W = &-\cos(114.09^o)\cdot U_1 - \cos(114.09^o)\cdot U_2 - \cos(35.26^o)\cdot U_3
\end{aligned}$$

These components are readily the velocity components in the wind tunnel coordinates system for which U corresponds to the streamwise direction (assuming the probe was aligned with the main flow direction when mounted in the wind tunnel).

Coordinates Transformation for Bi-axial Probe

In the case of a X-wires probe, the velocity components in the wire-coordinates system $\{U_1, U_2\}$ are given as (after inversion of the corresponding 2×2 matrix):

$$U_1 = \frac{\sqrt{2}}{2}\sqrt{(1+k^2)\cdot U_{cal2}^2 - k^2\cdot U_{cal1}^2}$$

$$U_2 = \frac{\sqrt{2}}{2}\sqrt{(1+k^2)\cdot U_{cal1}^2 - k^2\cdot U_{cal2}^2}$$

where k^2 has the same value as above ($k^2 = 0.04$). The velocity components in the probe-coordinates system $\{U, V\}$ read:

$$U = \frac{\sqrt{2}}{2}\big(U_1 + U_2\big)$$

$$V = \frac{\sqrt{2}}{2}\big(U_1 - U_2\big)$$

Note that in this report these components are further rotated so that the first component U is parallel to the airfoil surface and the second one V perpendicular to it (see Section 2.5). The third component is kept unchanged and is parallel to the trailing edge. The third component is actually measured by rotating the X-wire probe and is still obtained by using the latter coordinates transformation for bi-axial probe.

C Turbulence Theory Reminder

This appendix is a short reminder on turbulence theory that indicates how some of the results presented in this report are obtained.

The subscripts x, y and z refer to the streamwise and the two transversal flow directions, respectively. However, the indices 1, 2 and 3 are used interchangeably.

C.1 Correlation and Integral Length Scale

An integral scale can be defined as a measure of the longest correlation distance between two points in the flow that are separated either by space or time. In the present experimental set-up, the hot-wire measurements are performed at a single point in space during a given period of time. However, assuming Taylor hypothesis of frozen turbulence, an integral *length* scale can be evaluated.

For a given velocity component u_i ($i = x, y$ or z), the corresponding integral length scale is defined by:

$$L_i = \frac{1}{\sigma_i^2} \int_0^{+\infty} R_{ii}(r)\, \mathrm{d}r \tag{C.1}$$

The auto-correlation function is given as:

$$R_{ii}(r) = < u_i(\boldsymbol{x} + \boldsymbol{r}, t)\, u_i(\boldsymbol{x}, t) >$$

where r is the norm of the separation vector $\boldsymbol{r}$, $\boldsymbol{x}$ is an arbitrary space location, and the operator $< \cdot >$ denotes the ensemble average. Note that isotropy and stationarity were assumed here, such that the correlation tensor is a function of r only. The variance σ_i^2 is the mean square value of the velocity component u_i and is also given as:

$$\sigma_i^2 = R_{ii}(0)$$

In practice, the integral in Eq. (C.1) is evaluated on a finite interval $[0, r_0]$, where r_0 denotes the distance at which the correlation function first cancels. Indeed, integrating over the whole spatial domain would yield numerical inaccuracies that corrupt the results. It should be also noted that in the case of measured velocity time-series, the integration interval will necessarily be finite.

Using the Wiener-Khinchin theorem, the auto-correlation function can be defined as the Fourier transform of the velocity power spectrum as:

$$R_{ii}(r) = \frac{1}{2\pi} \int_{-\infty}^{+\infty} S_{ii}(k)\, \mathrm{e}^{\mathrm{i}kr} \mathrm{d}k$$

where k is the wavenumber and $S_{ii}(k)$ is the *wavenumber* power spectral density of the velocity u_i. The *frequency* power spectral density is obtained from the velocity time-series $u_i(t)$ as:

$$S_{ii}(\omega) = \hat{u_i}(\omega)\, \hat{u_i}^*(\omega)$$

where the upper star $*$ indicates the complex conjugation and $\hat{u_i}$ is the Fourier transform of the time-series. In the previous formula, the angular frequency ω is related to the wavenumber as:

$$k = \omega / U_c$$

according to the frozen turbulence hypothesis. The convective velocity U_c denotes the velocity at which turbulence is convected by the flow. In our case, the local averaged streamwise velocity is used. The wavenumber power spectral density is related to the frequency power spectral density as:

$$S_{ii}(k) = S_{ii}(\omega)\, U_c$$

Because of the isotropy assumption, the spectrum S_{ii} is related to the turbulent velocity spectral tensor $\mathbf{\Phi}$ as:

$$S_{ii}(k) = \Phi_{ii}(\boldsymbol{k})$$

where k is the norm of the wavenumber vector $\boldsymbol{k}$.

Note that an integral length scale L_{ij} based on two distinct velocity components u_i and u_j $(i \neq j)$ can also be defined. In this case, the auto-correlation function has to be replaced by the cross-correlation $R_{ij}(r)$, and the power spectral density by the cross-spectral density of the two components.

C.2 Isotropic Turbulent Flow and Spectra

The so-called Von Karman spectrum for the turbulent kinetic energy (TKE) has the following form:

$$E(k) = \alpha\, \epsilon^{2/3} L^{5/3} \frac{(Lk)^4}{(1+(Lk)^2)^{17/6}} \tag{C.2}$$

where $E(k)\,\mathrm{d}k$ is half the variance of the wind velocity fluctuations in the range $[k, k+\mathrm{d}k]$, that is:

$$\int_0^\infty E(k)\,\mathrm{d}k = k_T \tag{C.3}$$

where ϵ is the viscous dissipation rate of TKE k_T, L is the so-called outer integral scale (that defines the transition between the energy and the inertial subranges), and the scalar k is the norm of the wavenumber vector $\boldsymbol{k} = (k_1, k_2, k_3)$. Experimental measurements of atmospheric boundary layer turbulence suggest that the empirical constant α can be approximated by $\alpha \approx 1.7$. In some other cases [1] and in this report, the value 1.4528 is used as it ensures that the equality in Eq. (C.3) is readily satisfied when approximating the dissipation as a function of the velocity scale and integral length scale (see below).

Assuming that the energy-containing eddies break up at a time scale equal to their turn-over time, the dissipation can be approximated as:

$$\epsilon \approx \frac{u_0^3}{L} \tag{C.4}$$

where u_0 is the characteristic velocity of the large energy-containing eddies. It is related to the variance σ_{1c}^2 of one of the fluid flow velocity components as $\sigma_{1c}^2 = u_0^2 = \sigma^2/3$, where σ^2 stands for the total variance of the turbulent velocity assuming isotropy (i.e. $\sigma^2 = 2\,k_T$).

The one-point spectra of the velocity components, which are measured in practice (at one fixed point in space during a given time period - see above for the transformation from the frequency to the wavenumber spectra assuming frozen turbulence), are defined as a function of the spectral tensor as:

$$F_i(k_1) = \iint_{-\infty}^{+\infty} \Phi_{ii}(\boldsymbol{k})\,\mathrm{d}k_2 \mathrm{d}k_3 \tag{C.5}$$

for the three components (i.e. $i = 1, 2$ or 3).

The turbulent velocity spectral tensor $\mathbf{\Phi}$ takes the following form for an isotropic incompressible flow:

$$\Phi_{ij}(\boldsymbol{k}) = \frac{E(k)}{4\pi k^4}(k^2\delta_{ij} - k_i k_j) \tag{C.6}$$

Using this expression, combining with the Von Karman spectrum definition in Eq. (C.2) and approximation (C.4), and integrating over the $k_2 - k_3$ wavenumber space (see for example Lumley [13] for details) finally yield to the following expressions for the one-point spectra:

$$F_1(k_1) = \frac{9\,\alpha\,\sigma_{1c}^2}{55} \cdot L \cdot \frac{1}{\left(1+(Lk_1)^2\right)^{5/6}} \tag{C.7}$$

and:

$$F_2(k_1) = F_3(k_1) = \frac{3\,\alpha\,\sigma_{1c}^2}{110} \cdot L \cdot \frac{3 + 8(Lk_1)^2}{\left(1 + (Lk_1)^2\right)^{11/6}} \tag{C.8}$$

These functions, pre-multiplied by k_1, reach their respective maximum at the following values:

$$k_1|_{\max(k_1 F_1)} \approx 1.2247/L \quad \text{and} \quad k_1|_{\max(k_1 F_{2,3})} \approx 1.7824/L$$

Having measured the one-point spectra with the hot-wire device placed in the wind tunnel (and pre-multiplied with the streamwise wavenumber k_1), their maximum value can be located yielding estimated numerical values for the outer integral scale L using the relationships defined above. Note that it is here assumed that such a length scale can be independently defined for each of the three components components.

The outer integral scale L is defined as the inverse of the wavenumber of the energy-containing eddies k_e, that is:

$$L = 1/k_e$$

In addition, for isotropic turbulence, the integral length scale L_i (i=x, y or z) can be related to the previous wavenumber as [15]:

$$L_i \approx 0.7468/k_e \quad = 0.7468\,L \tag{C.9}$$

Combining the previous equations, three alternative definitions of the integral length scales can be obtained using the respective wavenumbers defining the maxima of the pre-multiplied one-point spectra as:

$$\widetilde{L}_x \approx 0.9147/k_1|_{\max(k_1 F_1)} \qquad \text{and} \qquad \widetilde{L}_{y,z} \approx 1.3312/k_1|_{\max(k_1 F_{2,3})} \tag{C.10}$$

C.3 General Spectral Form and Parameter Study

In the previous section, the so-called Von Karman spectrum was used as a model for the TKE spectrum. However, the low-wavenumber part of this spectrum is rather arbitrary since it may vary significantly from one particular flow condition to another. Indeed, the large turbulent structures are mainly determined by the actual flow boundaries and the turbulence generation mechanism. It seems that the spectrum proposed by Von Karman was primarily chosen on mathematical considerations as it provides analytical solutions for many integrals in the theory yielding concise theoretical results (see for example previous section).

Let now assume a more general form for the TKE spectrum:

$$E(k) = \alpha\,\frac{3}{2}\,\sigma_{1c}^2\,L\,f(\xi) \tag{C.11}$$

where $\xi = kL = \sqrt{k_1^2 + k_2^2 + k_3^2}\,L$ is the non-dimensional wavenumber, and the spectral functional form is given by the function:

$$f(\xi) = \frac{\xi^{n_E}}{\left(c_E + \xi^2\right)^{(3\,n_E+5)/6}} \tag{C.12}$$

where the parameters n_E and c_E can be arbitrarily chosen. The exponent $(3\,n_E + 5)/6$ in the denominator ensures that the spectrum presents a $-5/3$ slope decay at high wavenumbers in agreement with the existence of an inertial sub-range for the small scales of turbulence. The Von Karman spectrum is recovered with the following choice for the model parameters:

$$n_E = 4 \qquad \text{and} \qquad c_E = 1$$

To ensure that the energy contained is this spectrum is equal to the total TKE of the flow k_T, and assuming isotropy (i.e. $k_T = \frac{3}{2}\,\sigma_{1c}^2$), the constant α is given as:

$$\alpha = 1/\Big(\int_0^{+\infty} f(\xi)\,\mathrm{d}\xi\Big) \tag{C.13}$$

Parameters Influence on TKE spectrum

In order to evaluate the influence of the different parameters on the model, the following parametric study is performed. All parameters are varied around the following reference values:

$$n_E = 4\,, \qquad c_E = 1\,, \qquad \sigma_{1c}^2 = 1\,[(\mathrm{m/s})^2]\,, \qquad L = 10^{-3}\,[\mathrm{m}]$$

The results are shown in Fig. 37. It is important to note here that when modifying the n_E or the c_E parameter, the factor α is recalculated according to Eqs. (C.12)-(C.13) for each new case.

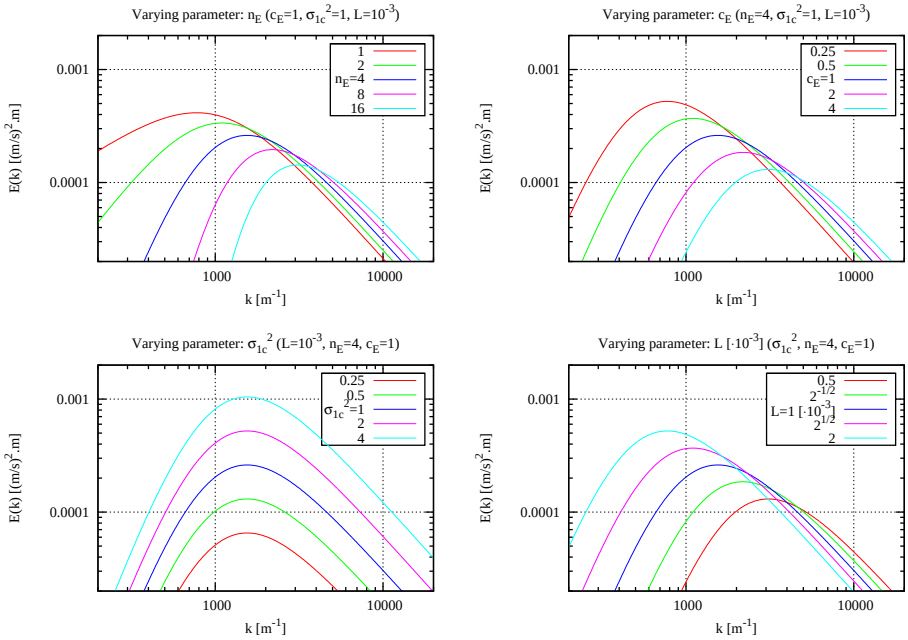

Figure 37. Parameter study for the TKE spectrum $E(k)$

It can be seen that decreasing the parameter c_E has an identical effect as increasing the outer integral scale L, namely shifting the spectrum peak wavenumber to lower values and increasing the associated spectrum peak value. Decreasing the parameter n_E has a similar effect on the high-wavenumber part of the spectrum. However, it also induces an increase of the energy contained at wavenumbers lower than the peak wavenumber by decreasing the local spectrum slope. Increasing the variance σ_{1c}^2 is merely shifting the spectrum upward.

Parameters Influence on Vertical Velocity Component Energy Spectrum

The spectrum of interest for the TNO model is the second diagonal component of the turbulent velocity spectral tensor $\Phi_{22}(\boldsymbol{k})$ which is obtained using Eq. (C.6) assuming isotropy:

$$\Phi_{22}(\boldsymbol{k}) = \frac{\alpha\,\frac{3}{2}\,\sigma_{1c}^2}{4\,\pi}\,L^3\,\frac{\xi_1^2 + \xi_3^2}{\big(c_E + \xi^2\big)^{a_E}\,\big(\xi^2\big)^{b_E}}$$

where $\xi_i = k_i L$ ($i = 1, 2$ or 3) and the exponents a_E and b_E read:

$$a_E = \frac{3\,n_E + 5}{6} \qquad \text{and} \qquad b_E = \frac{4 - n_E}{2}$$

However, before being used in the TNO model (see Appendix D), the previous spectrum has to be integrated with respect to k_2 as:

$$\widetilde{\Phi}_{22}(\boldsymbol{k}_{\parallel}) = \int_{-\infty}^{+\infty} \Phi_{22}(\boldsymbol{k})\,\mathrm{d}k_2$$

$$= \frac{\alpha\,\frac{3}{2}\,\sigma_{1c}^2}{4\,\pi}\,L^2 \int_{-\infty}^{+\infty} \frac{\xi_1^2+\xi_3^2}{\left(c_E+\xi_1^2+\xi_2^2+\xi_3^2\right)^{a_E}\left(\xi_1^2+\xi_2^2+\xi_3^2\right)^{b_E}}\,\mathrm{d}\xi_2$$

where $\boldsymbol{k}_{\parallel}=(k_1,k_3)$ is the wavenumber projected on the plane parallel to the wall surface. This integration can be performed analytically if $n_E=4$ (i.e. $a_E=17/6$ and $b_E=0$). In the general case, it has to be performed numerically.

The influence of the general model parameters on $\widetilde{\Phi}_{22}$ is displayed in Fig. 38. Note that the spectra are plotted as a function of $k_{\parallel}=\sqrt{k_1^2+k_3^2}$ since the spectrum is symmetric with respect to k_1 and k_3. The conclusions concerning the influence of the parameters are the same as for the spectrum $E(k)$ above.

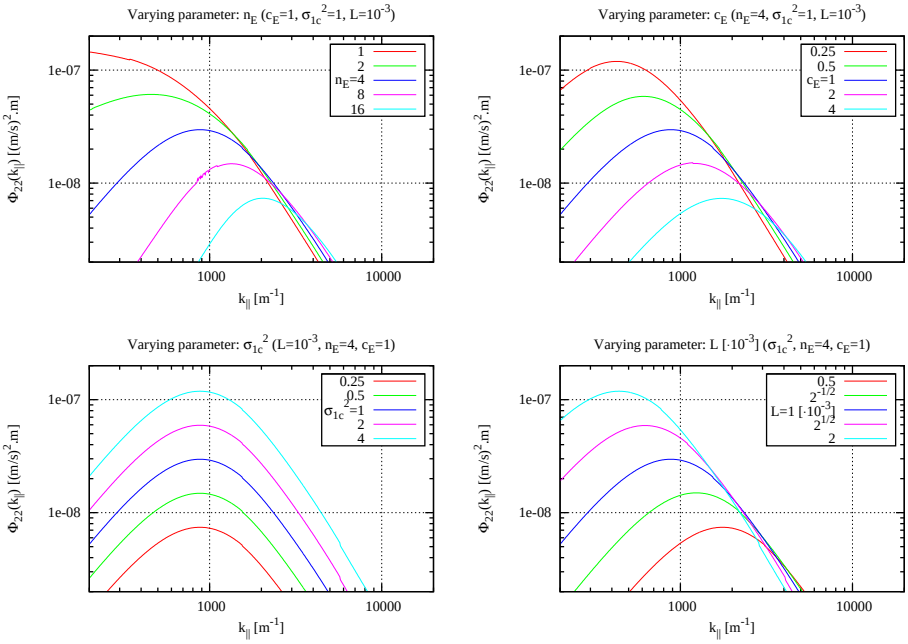

Figure 38. Parameter study for the vertical velocity energy spectrum $\widetilde{\Phi}_{22}(k_{\parallel})$

Parameters Influence on One-Point Spectrum

Finally, the model parameter study is performed for the pre-multiplied one-point spectrum $F_2(k_1)$ defined in Eq. (C.5). The results are displayed in Fig. 39. Again, varying the parameters c_E and L has identical effects, but now only the peak wavenumber is shifted. A similar effect is observed for the parameter n_E together with a slight reduction of the spectrum peak value when this parameter is decreased. The vertical shift of the spectrum observed earlier for the parameter σ_{1c}^2 is preserved.

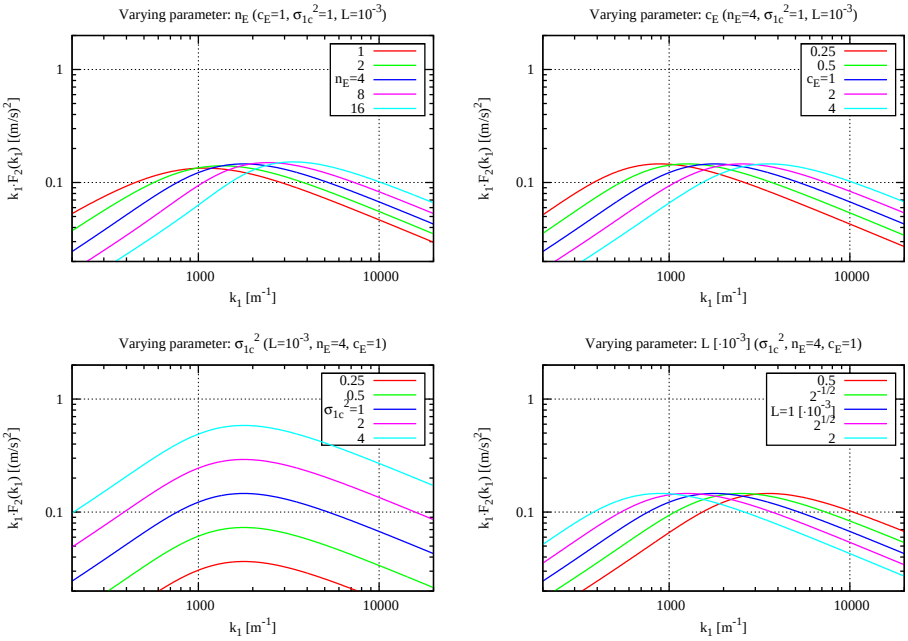

Figure 39. Parameter study for the pre-multiplied one-point spectrum $F_2(k_1)$

D TNO Trailing Edge Noise Model

This model which was originally proposed by Parchen [20] is gathering several from the previous results. These are used to formulate a far field noise level expression as a function of turbulent boundary layer quantities. These data can be collected from any fluid flow solver which includes a description of the turbulent boundary layer. For example, a panel method coupled to an integral boundary layer formulation as in the software XFOIL [7] can be used. Alternatively, any CFD code including a turbulence model for the boundary layer can be considered.

D.1 Model Formulation

The first part of the model is based on a formula expressing the contribution of the mean-shear/turbulence interaction in the boundary layer and which relates the turbulent boundary layer characteristic data to the fluctuating surface pressure (see Blake [3], Vol.II, p.513, p.524). Using the fact that the wavenumber-frequency spectrum of the wall pressure fluctuations is related to the modulus of its Fourier transform and manipulating, Parchen [20] arrived to the following result for the wavenumber-frequency surface pressure spectrum:

$$\Phi_p(\boldsymbol{k}_\parallel,\omega) = 4\,\rho_0^2 \frac{k_1^2}{k_1^2+k_3^2} \int_0^{+\infty} L_2(y_2) \left(\frac{\partial U_1}{\partial y_2}(y_2)\right)^2 \overline{u_2^2}(y_2)\, \widetilde{\Phi}_{22}(\boldsymbol{k}_\parallel) \times \Phi_m(\omega - U_c(y_2)k_1)\, \mathrm{e}^{-2\,k_\parallel y_2}\, \mathrm{d}y_2 \quad \text{(D.14)}$$

where $k_\parallel$ is the norm of the wavenumber $\boldsymbol{k}_\parallel = (k_1, k_3)$ spanning the plane parallel to the wall surface, L_2 is the vertical integral length which characterizes the vertical extent of the turbulent eddies, $\overline{u_2^2}$ is the mean squared value of the vertical velocity fluctuations, U_1 is the streamwise mean velocity (its derivative, the mean shear, actually appears in the integral), $\widetilde{\Phi}_{22}$ is the *normalized* spectrum of the vertical velocity fluctuations integrated over k_2, Φ_m is the so-called moving axis spectrum which describes how $\widetilde{\Phi}_{22}$ is distorted by the generation and destruction of eddies during their convection past the trailing edge, and U_c is the convection velocity of these eddies. It should be noted that $\widetilde{\Phi}_{22}$ depends on the outer integral scale L (see below) and thereby is also a function of y_2. In addition, remind that in the present section $\widetilde{\Phi}_{22}$ is normalized, the spectrum amplitude being explicitly introduced in the integral (D.14) through the $\overline{u_2^2}$ factor in contrast to Appendix C where the amplitude factor is integrated into $\widetilde{\Phi}_{22}$.

Before relating this wavenumber-frequency spectrum to the far field noise, the two spectra $\widetilde{\Phi}_{22}$ and Φ_m present in the integral across the boundary layer in Eq. (D.14) are expressed using results from turbulence theory.

The moving axis spectrum is assumed to be gaussian and takes the following form:

$$\Phi_m(\omega - U_c k_1) = \frac{1}{\alpha_{\text{Gauss}}\sqrt{\pi}} \mathrm{e}^{-[(\omega - U_c k_1)/\alpha_{\text{Gauss}}]^2}$$

where the gaussian constant α_{Gauss} is a function of the eddy convection velocity and turbulent length scale:

$$\alpha_{\text{Gauss}} = 0.05\, U_c / L_2$$

The convection velocity is itself a function of the local boundary layer velocity as:

$$U_c(y_2) = c_{\text{cv}}\, U_1(y_2)$$

where the constant c_{cv} is set equal to 0.7.

The Karman three-dimensional turbulent kinetic energy spectrum for isotropic turbulence reads:

$$E(k) = \frac{110\,\Gamma(5/6)}{27\sqrt{\pi}\,\Gamma(1/3)}\frac{k_T}{k_e}\frac{(k/k_e)^4}{[1+(k/k_e)^2]^{17/6}} \tag{D.15}$$

where $k_e = 1/L$ is the wavenumber of energy containing eddies, k_T the turbulent kinetic energy, and k the norm of the wavenumber $\boldsymbol{k} = (k_1, k_2, k_3)$ spanning the whole wavenumber space. From this equation, the energy density spectrum for the vertical fluctuations in the k_1-k_3 plane can be expressed, again assuming isotropy, as:

$$\widetilde{\Phi}_{22}(\boldsymbol{k}_\parallel) = \frac{4}{9\pi k_e^2}\frac{(k_1/k_e)^2 + (k_3/k_e)^2}{[1+(k_1/k_e)^2+(k_3/k_e)^2]^{7/3}} \tag{D.16}$$

after integration along k_2 (see Appendix C for more details).

The second part of the model consists in expressing the far field noise as a function of the previous wavenumber-frequency spectrum of the surface pressure fluctuations defined by Parchen [20]. Using the results of Chase [5] and Brooks and Hodgson [4], the far field pressure spectrum density can be expressed as an integral of the wall pressure spectrum over the wavenumber component in the flow direction:

$$S(\omega) = \frac{D}{4\pi R^2}\int_{-\infty}^{+\infty}\frac{\omega}{c_0\,k_1}\Phi_p(\boldsymbol{k}_\parallel,\omega)|_{k_3=0}\,\mathrm{d}k_1 \tag{D.17}$$

where R denotes the distance of the observer to the trailing edge, D the span extent of the trailing edge, and c_0 is the speed of sound.

The surface pressure frequency-spectrum is obtained by integrating Eq. (D.14) over the surface wavenumber space:

$$P_{\text{wall}}(\omega) = \iint_{-\infty}^{+\infty}\Phi_p(\boldsymbol{k}_\parallel,\omega)\,\mathrm{d}k_1\mathrm{d}k_3$$

At this point, the integral length scale L_2, the mean shear $\partial U_1/\partial y_2$, the wavenumber k_e, and the turbulent shear stress $\overline{u_2^2}$ still need to be specified in order to close the model. The specification of these quantities depends on the methodology that is used to calculate the flow field. Two approaches are considered: the integral boundary layer panel code XFOIL [7], and a Reynolds-Average Navier-Stokes solver (in our case EllipSys2D [17, 18, 22]).

D.2 Input from Integral Boundary Layer Method

In the case of a XFOIL calculation, boundary layer equations are solved in order to determine its development along the airfoil chord. This calculation is coupled to a panel method used to compute the inviscid flow outside the boundary layer. The data of interest that are given as an output from XFOIL are: the skin friction coefficient at the wall C_f, the momentum thickness θ, the displacement thickness δ^*, the velocity at the edge of the boundary layer U_0.

The missing data needed for the model proposed in the previous section are obtained using results from classical turbulent boundary layer theory, as well as isotropic turbulence.

The boundary layer thickness δ can be related to the momentum thickness and the displacement thickness by using the relation by Drela and Giles [8]:

$$\delta = \theta\left(3.15 + \frac{1.72}{H_k - 1}\right) + \delta^*$$

where $H_k = \delta^*/\theta$ is the kinematic shape factor which is also given as an output of XFOIL. The velocity profile can then be approximated in the boundary layer by using Cole's law of the wall/law of the wake [10] as:

$$U_1(y_2) = u^* \left(\frac{1}{\kappa} \ln \left(\frac{u^* y_2}{\nu} \right) + B + \frac{1}{2} W(y_2) \left(\frac{U_0}{u^*} - \frac{1}{\kappa} \ln \left(\frac{u^* \delta}{\nu} \right) - B \right) \right)$$

where $\kappa = 0.41$ is the Karman constant, $B = 5.5$, and $u^* = U_0 \sqrt{C_f/2}$ is the friction velocity. The wake function is defined as:

$$W(y_2) = 1 - \cos(\pi y_2/\delta)$$

The velocity profile formula can easily be derived with respect to y_2 to obtain the mean shear.

The next quantity to be defined is the integral length scale L_2. In a first step, the mixing length scale expression proposed by Schlichting [21] is used:

$$l_m = 0.085\,\delta \tanh \left(\frac{\kappa\, y_2}{0.085\,\delta} \right)$$

Then, the integral length is approximated as:

$$L_2 = \frac{l_m}{\kappa} \tag{D.18}$$

In the case of isotropic turbulence (such an assumption is here needed in order to get the following approximation), the integral length is well defined and related to the wavenumber of the energy-bearing eddies as:

$$L_2 = \frac{\sqrt{\pi}\,\Gamma(5/6)}{\Gamma(1/3)} \frac{1}{k_e} \tag{D.19}$$

yielding:

$$k_e \approx 0.7468/L_2$$

which can be used for evaluating the normal velocity fluctuations spectrum $\widetilde{\Phi}_{22}$ in Eq. (D.16).

The last quantity to be defined is the turbulent shear stress. Prandtl's mixing length hypothesis assumes that the turbulent viscosity ν_t is related to the mixing length and the mean shear as:

$$\mu_t = \rho\, l_m^2 \left| \frac{\partial U_1}{\partial y_2} \right|$$

Then, the turbulent kinetic energy k_T is given by:

$$k_T = \sqrt{\left(\mu_t \frac{\partial U_1}{\partial y_2} \right)^2 / C_\mu} \tag{D.20}$$

where $C_\mu = 0.09$. The turbulent shear stress is then assumed proportional to the turbulent kinetic energy as:

$$\overline{u_2^2} = \beta\, k_T \tag{D.21}$$

where the constant $\beta = 0.45$ on the suction side, and $\beta = 0.3$ on the pressure side of an airfoil. Note that this factor has been tuned to fit some experimental results [20].

D.3 Input from RANS Calculation

In the case of a RANS code is used, many of the previous model input data are directly accessible from the computed quantities. In particular, the velocity profile, and thereby the mean shear, accross the boundary layer can be extracted from the velocity field at the trailing edge. Similarly, the turbulent kinetic energy k_T

(as well as its dissipation rate ϵ) can be interpolated along the same boundary layer path. Eq. (D.21) is then used to obtain the turbulent shear stress $\overline{u_2^2}$.

The integral length scale is the last remaining quantity to be defined. Wagner *et al* [23] used the simple assumption that the vertical correlation length is proportional to the mixing length scale as in Eq. (D.18).

Lutz *et al* [14] argues that the determination of the vertical length scale is most crucial for the consistency of the noise prediction. Therefore, a more elaborate approach to evaluate L_2 is proposed. In the case of isotropic turbulence, the integral length is well defined as a function of the wavenumber of the energy-bearing eddies as:

$$L_2 = \frac{\sqrt{\pi}\,\Gamma(5/6)}{\Gamma(1/3)}\frac{1}{k_e} \approx 0.7468\,\frac{1}{k_e}$$

The Kolmogorov spectrum in the inertial subrange reads:

$$E(k) = C\,\frac{\epsilon^{2/3}}{k_T^{5/3}}$$

where the constant $C \approx 1.5$ was experimentally determined, and ϵ is the turbulent energy dissipation rate. By comparing the previous spectrum with the asymptotic behavior of the Karman spectrum in Eq. (D.15), the wavenumber of the energy bearing eddies k_e can be deduced:

$$k_e \approx 1.9275\,\frac{\epsilon}{k_T^{3/2}}$$

Combining this equation with the above equation relating the wavenumber k_e and the integral length L_2 in the case of isotropic turbulence, the following result can be established:

$$L_2 \approx 0.387\,\frac{k_T^{3/2}}{\epsilon} \tag{D.22}$$

This latter approach is used in the present report for calculations based on RANS computational results (instead of using Eq. (D.18)).

Note that in the original model proposed by Parchen [20], an alternative approximation for the vertical integral length scale that can be employed in conjunction with a Reynolds-Averaged Navier-Stokes solution method was proposed. The mixing length is first approximated by:

$$l_m = \frac{C_\mu^{3/4}\,k_T^{3/2}}{\epsilon}$$

Then, combining with Eq. (D.18) relating the mixing length scale to the integral length scale yields:

$$L_2 \approx 0.401\,\frac{k_T^{3/2}}{\epsilon}$$

which is very similar to Eq. (D.22).

Risø DTU is the National Laboratory for Sustainable Energy. Our research focuses on development of energy technologies and systems with minimal effect on climate, and contributes to innovation, education and policy. Risø has large experimental facilities and interdisciplinary research environments, and includes the national centre for nuclear technologies.

Risø DTU
National Laboratory for Sustainable Energy
Technical University of Denmark

Frederiksborgvej 399
PO Box 49
DK-4000 Roskilde
Denmark
Phone +45 4677 4677
Fax +45 4677 5688

www.risoe.dtu.dk